Universiteit
Leiden
The Netherlands

Exploring structure dependencies of gas-surface interactions with curved single crystals

Auras, S.V.

Citation

Auras, S. V. (2021, March 11). *Exploring structure dependencies of gas-surface interactions with curved single crystals*. Retrieved from https://hdl.handle.net/1887/3151627

Version:	Publisher's Version
License:	Licence agreement concerning inclusion of doctoral thesis in the Institutional Repository of the University of Leiden
Downloaded from:	https://hdl.handle.net/1887/3151627

Note: To cite this publication please use the final published version (if applicable).

Cover Page

Universiteit Leiden

The handle https://hdl.handle.net/1887/3151627 holds various files of this Leiden University dissertation.

Author: Auras, S.V.
Title: Exploring structure dependencies of gas-surface interactions with curved single crystals
Issue Date: 2021-03-11

2

RECENT ADVANCES IN THE USE OF CURVED SINGLE CRYSTAL SURFACES

In surface science, research traditionally employs macroscopically flat surfaces of single crystals. Curved surfaces have been applied more sporadically, but their history stretches back for many decades. Realization of the potential benefits and practical applications in surface physics and surface chemistry research progressed slowly in the 20th century. In more recent decades, research employing partial cylinders and dome-shaped crystals have found renewed interest. Modern surface sensitive techniques are being employed allowing the inherent large range of surface structures to reveal new insights. We briefly review the history, describe several types of surfaces and the range of structures they contain, suggest a notation for common types of curved surfaces, and discuss recent studies in more detail. We mainly focus on metal samples. We close with a short outlook.

This chapter is based on the following publication:
S. V. Auras and L. B. F. Juurlink. Recent advances in the use of curved single crystal surfaces. *Progress in Surface Science*, submitted.

2.1. INTRODUCTION

WHY USE SOMETHING OTHER than the well-defined, single surface structure offered by a near-perfectly flat polished single crystal? Flat samples are easily available in all kinds of shapes and sizes, and there is an enormous amount of experience built up over decades by the large surface science community in proper handling of these samples. There are well-defined cleaning procedures and one maximizes surface area with uniform structure at the atomic level. Surfaces with curvature may host a range of surface structures, but these may suffer from faceting and other forms of surface rearrangements that locally alter the ideal or expected bulk surface termination. Such non-continuous variations in surface structure needs to be dealt with and, at least, adequately studied. A large enough range of structure variations also requires larger samples and non-standard polishing techniques. Finding cleaning procedures that work properly for the entire range of surface structures present on a curved surface may also be nearly or entirely impossible, at least without inducing reconstructions of faceting somewhere along the surface. Larger samples also add experimental complexities as these are more difficult to heat and cool uniformly.

Regularly, researchers that attempted to reap the fruits of the single largest benefit of curved surfaces in modern scientific research - i.e. hosting a large range of surface structures in a single single crystal - speak of the technical difficulties. To investigate effects of terrace size, edges and kinks or corner atoms, one could revert to the use of nanocrystals. These may inherently contain various facets and 'defect' types and densities. Indeed, the use of nanoparticles grown on well-defined supports has shown to provide this option with high levels of control over crystal shape and size.[1] However, remaining heterogeneity and limited surface area may be reason to revert back to single crystals and consider using a curved surface instead of a flat surface to introduce controled variation of surface structure. The use of curved surfaces is now nearly 100 years old and still going strong, albeit well under the radar for many surface scientist raised with the idea that flat surfaces are the only norm. For those unfamiliar to the field, many types of continuously curved single crystal shapes have been made and used: spheres, solid and hollow full cylinders, partial cylinders, inverted cylinders, domes and cones. The history of surface science is long enough that pretty much every shape has been used, often for a particular reason. Figure 2.1 shows a small collection crystal shapes that have appeared in the 20^{th} century literature on metal curved surfaces.

This review starts with a brief historical overview of the use of curved surfaces of single crystals in surface science. It mostly pays homage to predecessors by illustrating studies prior to the widespread application of Scanning Tunneling Microscopy (STM). The following section has a pedagogical intention. It illustrates through examples which range of ideal truncations of bulk crystal structures may appear on commonly

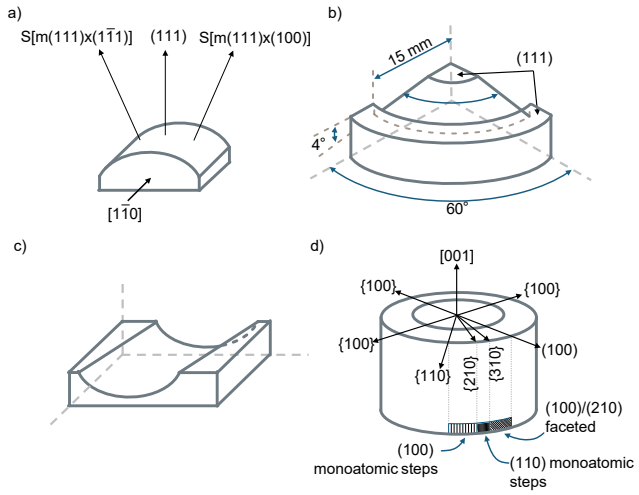

Figure 2.1: Examples of curved crystal shapes used in research in the 20th century. The solid sections of a Pt and Au cylinders included ~ 14°.[2] The conical [3] and extracted cylindrical [4] shapes were made from Cu single crystals. The full hollow Pt cylinder showed both monoatomic stepped and faceted regions.[5] Images are redrawn from original figures with minor alterations for clarity.

used shapes and sizes of curved single crystal surfaces. We propose a new notation that captures most commonly used crystal shapes for which one also easily extracts the available range of surface structures. We subsequently discuss recent studies and the advancements in the field in the last 20-25 years. We conclude with a short outlook.

2.2. BRIEF HISTORICAL OVERVIEW

At least as early as 1927 have properties of curved surfaces of clean metallic single crystals been studied. Ernest Linder at the State University of Iowa investigated the emission of electrons from a zinc single crystal rod under ultraviolet irradiation in vacuum.[6] The rod was cleaned by evaporating the outer layers of the moulded single crystal. To do so, Linder had to heat the entire glass vacuum apparatus, including the 4 cm long cylindrical Zn single crystal, to 400 °C with a Bunsen burner while ensuring that windows and other important parts did not get coated with Zn. He subsequently illuminated a 1 mm wide stripe along the cylinder's axis using light from a mercury arc lamp. The obtained photoelectric current varied a factor of 2 over a 90° rotation along the cylindrical axis of the sample. Linder suggested that it reflected the dependence of the work function on surface structure.

Around the same time, Hausser and Scholz at Siemens in Germany developed ways to grow macroscopic metallic single crystals in vacuum.[7] Sharing their Cu samples with Tammann and Sattorius at Göttingen University [8], they studied lattice struc-

tures and anisotropic behavior along the crystallographic axes using optical reflection and x-ray diffraction. Combining their observations with symmetry considerations, they arrived at conclusions regarding the dynamics of crystal growth and differences between ideal and real crystal structures.

Experimental techniques improved and at the end of the 1930's Martin at MIT's new George Eastman Laboratory imaged thermionic emission from a tungsten single crystal sphere of ~ 1 cm diameter in an apparatus originally designed by Shockley.[9] Photographs of patterns appearing on a bulb-shaped fluorescent screen illustrated the dependence of electron emission on crystallographic direction.

In subsequent years, chemists focused increasingly on dependencies of catalytic properties on surface structure. Improving crystal growth techniques and preparation of surfaces [10], Gwathmey and Benton showed that such dependencies occurred in reactions of O_2 and H_2 with copper spherical single crystals.[11, 12] They arrived at their conclusions based on experiments using no more than reflection of light from incandescent light bulbs and reporting color changes.[11, 13] Allen Gwathmey continued this work for many years to come, e.g. measuring relative rates for hydrogen oxidation on Cu(111) and Cu(100) planes.[14] Having noticed oxide formation, its dependence of crystallographic plane, and its effect on chemical reaction rates, he started combining research on spherical samples with flat single crystals. Both were produced by machining Cu rods grown under vacuum conditions. He also created larger flat areas on the surface of a Cu sphere, exposing surfaces, e.g. (100) and (111). Research on Cu oxidation and water formation went on [15] and expanded into the effect of impurities, e.g. Ag and Zn. These were added to the surface by electrodeposition, evaporation, or dipping the spheres in solutions containing the metal of interest.[16] An ellipsometer was constructed to measure surface structure dependent rates of oxidation [17] on flattened parts of Cu spherical crystals. X-Ray techniques were implemented to study the structure of Cu_2O grown by oxidation of spheres.[18] Gwathmey also studied catalytic reactions on Ni spheres [19, 20] and used spherical crystals to study friction and its dependence on surface structure.[21] The second PhD student that Allen Gwathmey worked with, Henry Leidheiser, also continued research on spherical crystals, e.g.. on the phase transition in Co [22] and catalytic reactions on its surface [23], and on the structure dependence of rate of development of silver chloride surfaces.[24]

More research groups picked up on the potential of curved surfaces in the last three decades of the 20^{th} century. The growing number of available experimental techniques and obtainable spatial resolution made the combination with curved surfaces of increasing interest to surface scientists. Wagner and coworkers in Jülich, Germany, used a 0.2 mm diameter electron beam from a LEED apparatus with partially curved W, Pt and Au samples and found a linear dependence of the work function with step density for these metals.[2] The dependence was attributed to the lowered dipole mo-

ment of steps in comparison to the low Miller index plane. At the Ecole Nationale Supérieure de Chimie in Paris, Domange and coworkers applied LEED and RHEED to study Cu vicinal surfaces.[3, 4, 25] They used crystals with multiple flattened parts at different relative angles and pioneered the use of smoothly curving conical samples. They also used a semiconducting GaAs crystal, predecessing extensive studies of such materials with curved shapes by Ranke.[26–28]. Bauer and coworkers in Clausthal, Germany, were the first to visualize how spot splitting in Low Electron Diffraction (LEED) patterns indicated a smoothly varying terrace width average over a 90° rotation, here for a W cylinder.[29] Spot splitting in LEED patterns of vicinal surfaces had only recently been explained by Ellis and Schwoebel as resulting from the interference between diffraction from the atomic low Miller index structure and step arrays.[30] For Bauer's W cylinder, it indicated stability of very rough surfaces with respect to faceting for the clean metal. In contrast, deposited Au overlayers diffused and formed faceted regions on parts where the W support showed high step densities. [31]

Beyond electron-based techniques, also H^+ ion scattering was applied to a study curved surfaces. Frenken and colleagues at AMOLF in Amsterdam used ion shadowing and blocking to study surface disordering (melting) and related it to the free energy difference between the solid and liquid states.[32] This difference varies with the local surface structure and explained (in part) their results for structure-dependent surface melting of a curved Pb sample.

Chemical properties and their importance to surface reactions were also explored in increasing detail in these decades. Probably being the first to employ a Pt curved sample, Comsa and coworkers in Jülich investigated O_2 and CO adsorption and reaction. [33] They reported that a LEED study of the clean crystal showed the expected variation in spot splitting, later published graphically for W by Bauer. Using Auger Electron Spectrscopy (AES) and a quadrupole mass spectrometer (QMS), subsequent experiments revealed a complex dependence of O_2 adsorption and CO oxidation reaction rates to surface structure. The two parallel mechanisms active in CO oxidation for Pt steps and (111) terraces were only very recently resolved by Wodtke and coworkers. [34]

Following Comsa's initial catalytic studies, Woodruff and coworkers at the University of Warwick in the UK used quantitative AES measurements and full cylindrical Cu and Ni samples. They studied surface structure dependencies in the absorbed and scattered electron currents and related them to variations in AES signal intensities. These were subsequently used to quantitatively relate dissociation kinetics of S_2, O_2 and N_2O to surface structure. [35–39].

Adding a rotatable Kelvin probe and photoemission electron microscopy (PEEM) to the list of employed techniques, Imbihl and Ertl used a full Pt cylinder to study struc-

ture dependencies in kinetic oscillations and spatiotemporal patterning in reactions of CO and NO under low vacuum conditions. [5, 40–43] With PEEM they obtained a spatial resolution of ~1 μm. They reported significant faceting along parts of the cylindrical surface, though, which may be related to their choice of the [001] direction of the Pt cylinder's rotational axis and the consequential combination of {100} and {110} planes making up the crystal's curved surface.[5]

One may expect that the invention of the STM in the early '80s was quickly applied in studies of curved surfaces. While LEED mostly provides averaged information on surface structure within the region probed by the relatively sizeable electron beam, STM yields structural information with much higher spatial resolution. Oddly, it took more than two decades before the first article appeared reporting a systematic STM study of surface structure variation along a curved surface. Results from the more recent decades by Bader, Fradin, and coworkers, by Ortega and coworkers, Gellman, Sykes and co-workers and our own will be discussed later. First, we consider the various surface structures and structural ranges obtainable using various crystal shapes for common unit cells of transition metals.

2.3. SURFACE STRUCTURES ON CURVED SURFACES OF SINGLE CRYSTALS

Macroscopically flat single crystals that are most commonly used in surface science studies are oriented, cut and polished to expose a single surface structure. Often an atomically flat, highly symmetric surface is chosen - a low Miller index plane. To consider surface structures exposed on a smooth curved surface, we find it most intuitive to start our consideration from such common low Miller index planes. They also often appear at the apex of partially curved samples.

For metals with a face-centered cubic (*fcc*) lattice, commonly used low-Miller index planes are the most densely packed hexagonal (111) and the more open square (001) surfaces. Figure 2.2a) and b) demonstrate their orientation within the *fcc* unit cell. Vectors drawn within the low Miller index plane indicate two azimuths pointing along different step structures. Alternatively, they may be considered two rotational axes for curved or cylindrical surfaces leading to ideal step structures as derived from the ordering of lattice points. The azimuths are 90° (30°) degrees apart for (111) and 45° degrees for (001). Figure 2.2c) and d) show two atomically flat planes in, respectively, *bcc* and *hcp* unit cells. While the first has a centered rectangular Bravais surface lattice, the second is hexagonal. Arrows again indicate two azimuths pointing along step directions or high-symmetry rotational axes. Note that, although *hcp*(0001) and *fcc*(111) are both hexagonaly close packed surfaces, stacking of subsequent atomic layers varies. While *hcp* has an A-B-A-stacking, *fcc* has A-B-C-A-stacking. This has consequences for the different types of steps appearing along a curved surface.

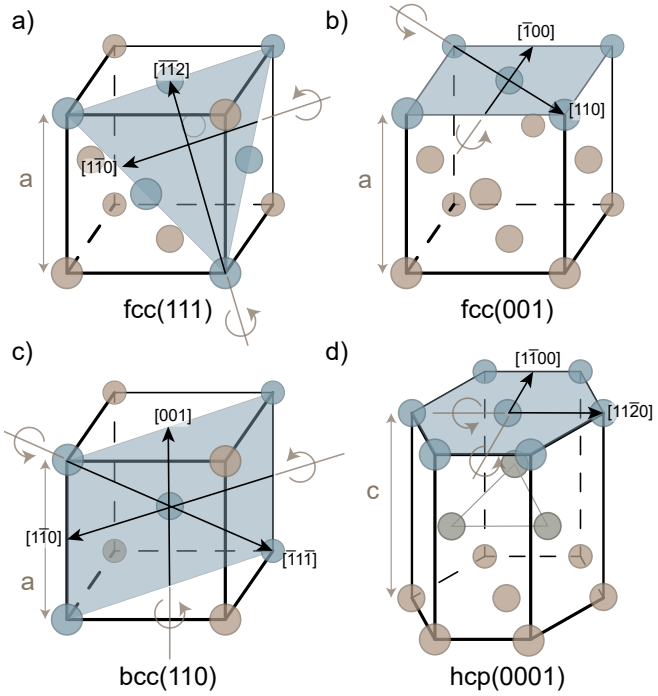

Figure 2.2: Unit cells of *fcc*, *bcc*, and *hcp* lattices and commonly used surface planes. The lattice constant a is indicated for the cubic unit cells. For *hcp* the second lattice constant c equals $\sqrt{\frac{8}{3}} \cdot a$. Blue arrows represent surface normals of the colored planes. Black arrows identify typical step directions and common rotational axes in curved and cylindrical samples. a) Hexagonal *fcc*(111) plane with close-packed A- and B-type step ([1$\bar{1}$0]) and fully-kinked step ([$\bar{1}\bar{1}$2]) directions. b) Square *fcc*(001) plane with close packed A'-type ([110]) and fully kinked step ([$\bar{1}$00]) directions. c) Centered rectangular *bcc*(110) plane with two achiral kinked step directions ([001] and [1$\bar{1}$0]). d) Hexagonal *hcp*(0001) plane with close-packed ([1$\bar{1}$00]) and kinked ([11$\bar{2}$0]) step directions.

For an ideally truncated surface, rotation from a low-Miller index plane introduces monoatomic steps. These steps separate terraces of the low-Miller index plane. With increasing angle, terraces are more frequently interrupted by steps, i.e. the step density increases and the average terrace width decreases. Rotation around different axes introduces different types of steps. They are characterized by the atomic arrangement in the step facet. In the case of single or double atomic steps, they are generally simply a microfacet of the first low-Miller index plane occurring on the arc between the surface normal and the azimuth. For example, in figure 2.2a), upward rotation of the (111) plane along $[1\bar{1}0]$ creates an arc connecting [111] to the $[\bar{1}\bar{1}2]$ azimuth. This arc passes through [001]. The atoms forming the microfacet are arranged in the same square manner as the (001) plane. This step type is often referred to as the A-type step. Downward rotation of the (111) plane along $[1\bar{1}0]$ passes through the (110) and, subsequently, $(11\bar{1})$ planes. The atomic ordering in the steps introduced into the (111) plane may thus be described as either a rectangular {110} or a hexagonal {111} microfacet. This type of step is generally referred to as the B-type step. In a similar fashion, different step facets connecting various types of planes may be derived from figure 2.2. Note that we here assume monoatomic steps. They are the shortest possible microfacet of a specific type. Step doubling is a term used to indicate that the microfacet stretches across two planes parallel to the surface. Stronger restructuring of a surface may expose large facets of (possibly) other planes than the microfacet of a monoatomic or double step. They are often the plane with the lowest free energy of the material. Although such faceting occurs, we focus here on monoatomic steps.

Figure 2.3 visualizes several different types of monoatomic steps by top view representations of domes with apices chosen identical to the planes indicated in figure 2.2. On (111) terraces of *fcc* metals, six directions of close-packed steps are possible. Figure 2.3a) shows the three equivalent directions exposing {001} microfacets (A-type steps) and three equivalent directions exposing {110} microfacets (B-type steps). Blue and red lines mark monoatomic steps. A closer look at the atomic arrangements of A- and B-type steps is given in figure 2.4. Color coding is maintained between these figures. In figure 2.4a), the step edge colored in red also illustrates how this B-type edge can be seen both as a {110} and {111} microfacet. For the latter, the lower (111) plane stretches one atomic row further into the edge than for the former.

Azimuthal directions in between two close-packed step types require kinks to be introduced in monoatomic steps. Taking the example of figure 2.3a) and figure 2.4a), {001} and {110} microfacets are connected alternately by outer and inner kinks. The highest repetition of kinks, i.e. the most corrugated edge, is formed with the shortest possible alternation of these type step sections. It is represented in purple in these figures. In between the most corrugated and the close-packed step types, the edges are in principle composed of longer stretches of one close-packed step type with less frequently occurring kinks and shorter stretches of the other close-packed step type.

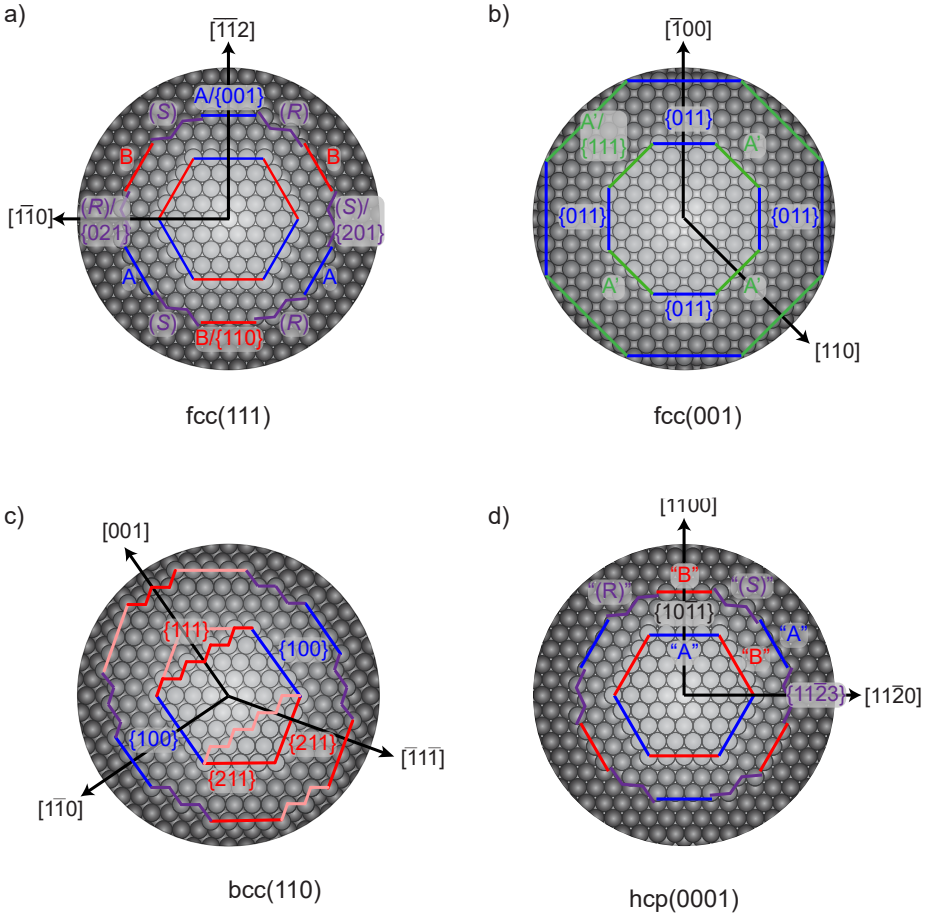

Figure 2.3: Top views of the atomically flat terraces of *fcc*, *bcc*, and *hcp* and possible step types. The displaed surface planes step down twice from the center towards the edges. a) Due to the hexagonal symmetry of *fcc*(111) terraces, three equivalent directions of {001}/A-type (blue) steps and {110}/B-type (red) steps are present. In between the close-packed step types, kinked steps can be found, consisting of A- and B-type segments separated by kinks. The resulting chirality (*(R)* or *(S)*) of stepped surfaces of this kind is indicated. Purple lines give directions of the fully kinked steps with equal lengths of A- and B-type steps. b) On *fcc*(001) terraces, four equivalent directions of close-packed {111}/A'-type steps can be found (green). Steps in between these orientations (blue) feature kinks separating short {111} segments, but do not inevitably cause chiral surfaces. c) On *bcc*(110) terraces, close-packed {211}-type steps (red) can be formed in four (not evenly spaced) directions. These types of close packed steps are inherently chiral. More open non-kinked steps are formed by {100} microfacets (blue) and are non-chiral. In between {211} and {100} directions, kinked steps form chiral surface. In between two adjacent {211} directions, a different type of kinked step (light red) is formed that does not automatically lead to chiral surfaces. d) On *hcp*(0001) terraces, six equivalent close packed step orientations are formed ({1011} microfacets). In subsequent steps of the same orientation, the step structure switches between arrangements like the *fcc* A-type and arrangements like the *fcc* B-type. In between close-packed step orientations kinked steps are formed, creating racemic surfaces.

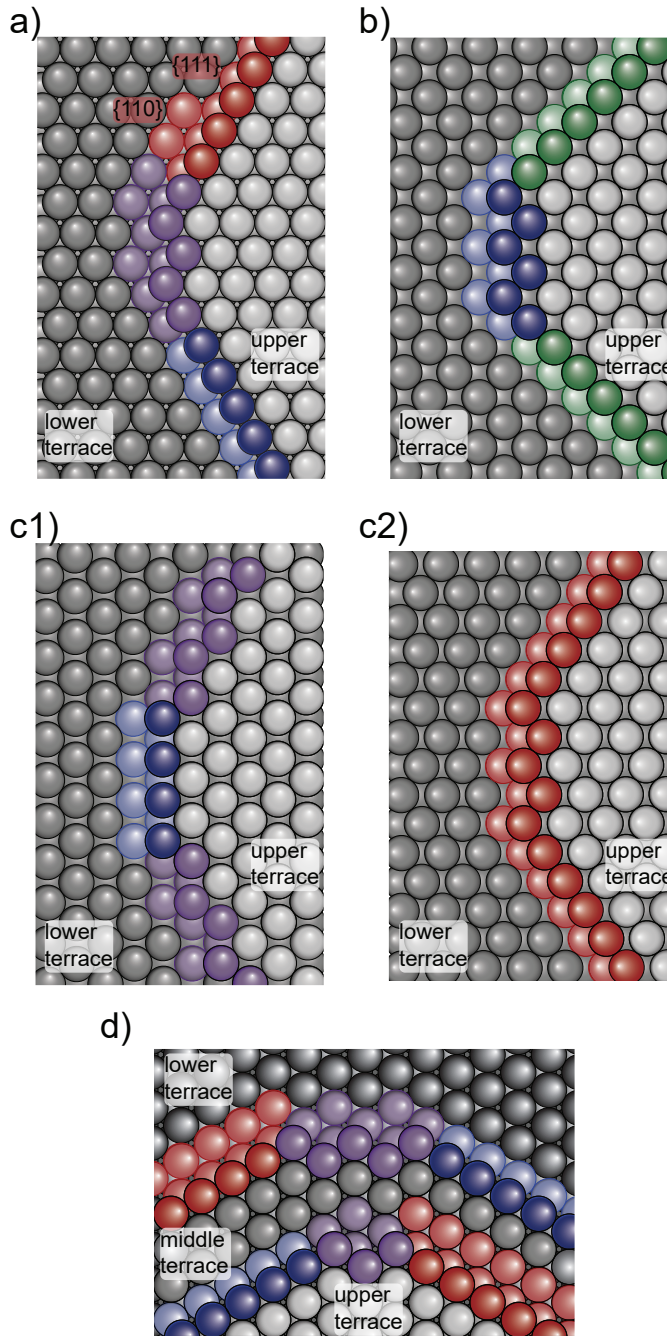

Figure 2.4: Atomic arrangement of different step types on a) *fcc*(111): A-type(blue), B-type(red), kinks(purple), b) *fcc*(001): A'-type (green), kinks (blue), c) *bcc*(110) c1): {100} steps (blue) and kinked steps consisting of {100} and {211} microfacets c2) Two {211} steps separated by a kinked achiral {111} step d) *hcp*(0001) close packed steps with A- and B-like structures on subsequent terraces, kinked step edges causing racemic surfaces.

The symmetry of kinked step edges is reduced compared to the close packed step edges. On stepped *fcc*(111) terraces this leads to chirality. While different nomenclatures have been proposed([44–46]), the established nomenclature uses the ordering of the Miller indices of the microfacets forming the inner kink. They are arranged by their atomic density (highest to lowest).[47] For terraces of *fcc*(111) with kinked steps, the three relevant microfacets are {111} for the lower terrace, and {001} and {110} for the edge segments forming the inner kink. Tracing the facets in the order of decreasing atomic density, i.e. {111} to {100} to {110}, gives a right-handed (*R*) or left-handed (*S*) rotation.[48] In figure 2.3a), the location of these *(R)* and *(S)* kinks are indicated. Figure 2.4a) shows the (R) version in between sections of A- and B- types steps. Kinked steps may partially reconstruct to reduce corrugation, but chirality is maintained.[49]

In contrast to (111) planes of the *fcc* unit cell, four equivalent directions yielding close-packed steps occur on (001) terraces, as displayed in figure 2.3b). They are {111} microfacets, or A'-type steps.[50] The inner corner of the step is identical to the A-type step, but the planes forming terrace and step are switched. In between the four equivalent azimuths, kinked steps are expected. Figure 2.4b) shows the atomic arrangement of A'-type steps, as well as fully-kinked steps in between the close-packed step orientations. Here, both sides of the inner kink are {111} microfacets. Chirality only occurs if unequal lengths of {111} facets separate the kinks. For a more detailed discussion on chirality of surfaces of different crystal lattices, we refer the reader to the roadmap laid out by Jenkins and Pratt.[46]

For the *bcc*(110) plane in figure 2.3c), we find the close packed steps forming {211} microfacets, as well as more open, but not kinked {100}-type steps, and different types of kinked steps. Kinked steps can be formed either from alternating segments of {211} microfacets and {100} microfacets, or by segments of {211} microfacets to both sides of a kink. The latter type of kinked step can be described as a {111}-type step. Figure 2.3 c) elucidates the orientation of different step types on a *bcc* (110) surface. It is noteworthy that stepped surfaces with {211}-type steps are chiral surfaces, despite the absence of kinks. This is due to the alignment of (110) planes, causing the atoms at the lower step edge to be slightly off-center relative to the upper step edge. Again, we refer to Jenkins and Pratt for detailed symmetry considerations.[46]

Lastly, step orientations on *hcp*(0001) resemble those of *fcc*(111) at first glance. Two close packed step types show the same arrangement as A- and B-type steps on *fcc*, we will therefore refer to them as such. However, subsequent steps in the same direction, show alternating A- and B-type steps, and as a result, curved crystals can never expose only one type of step. Consequently, the kinked steps at orientations away from the close-packed steps also alternate between *(R)* and *(S)* chirality, meaning that stepped surfaces involving kinks are always racemic surfaces.

2.4. CURRENTLY USED CRYSTAL SHAPES

In the absence of surface reconstructions, a macroscopic perfect sphere exhibits all possible terminations of the crystal lattice on its surface. Clearly, when performing research on the surface structure dependencies, this would be ideal. However, creating a perfectly polished single crystal sphere is rather complex. As discussed in section 2.2, single crystal spheres were used in experiments in the 20th century, but generally in an "as-created" spherical shape from a melt. Such spheres are often faceted away from low-Miller index planes and therefore do not exhibit a truly smooth and continuous range of step densities. In addition, spherical samples are also difficult to handle experimentally in modern surface science equipment, which are generally designed for studies of flat single crystal surfaces.

Instead of full spheres, dome-shaped samples, as schematically illustrated in figure 2.3, and (sections of) domes can be more easily implemented.[51] Figure 2.5 shows photos of dome-shaped crystals used by two separate groups in recent years. Domes maintain curvature in both directions, which allows studying a range of surface structures with large variations in both step and kink densities. With sizes comparable to standard flat single crystals, they are experimentally quite easily implemented. At the same time, curvature in two directions lowers surface area with a unique surface surface structure, thus requiring surface sensitive techniques with a small footprint. Scanning tunneling microscopy and electron- or ion based probes with a small beam focus are particularly suited to study dome-shaped crystals. Images from crystals as currently still in use by Sykes (Tufts University) and Gellman (Carnegie Mellon) are shown in figure 2.5b). Crystals as used by Qiu and Bader near the turn of the century are shown in figure 2.5c). Their samples are 10 mm in diameter with varying levels of curvature. The crystal from Qiu spans ~15°, whereas the Gellman crystals span 28°. The inherent (*R*) and (*S*) chirality of kinked steps is indicated in the image from Gellman.

Reducing the curvature to only one dimension, as done with a (part of a) cylinder, fixes the step type and surface structure along the cylindrical axis, but allows variations of step density along the curvature. Therefore, the same surface structure can be probed across the width of the sample and spatial resolution only has to be high in the direction of curvature. This still requires adaptions to most UHV surface science techniques, as they usually probe a circular area on a flat sample, but significantly improves signal-to-noise ratios for some surface sensitive techniques. For example, adsorption and desorption measurements relying on the use of a quadrupole mass spectrometer benefit from larger areas with uniform surface structure.

Cylindrical samples maintain the full 360° rotation of a complete sphere, but appear rather difficult to use in pre-exisiting ultra-high vacuum systems. Such crystals were used with a diameter on the order of 20 mm and a height of 10-20 mm in the 1980's

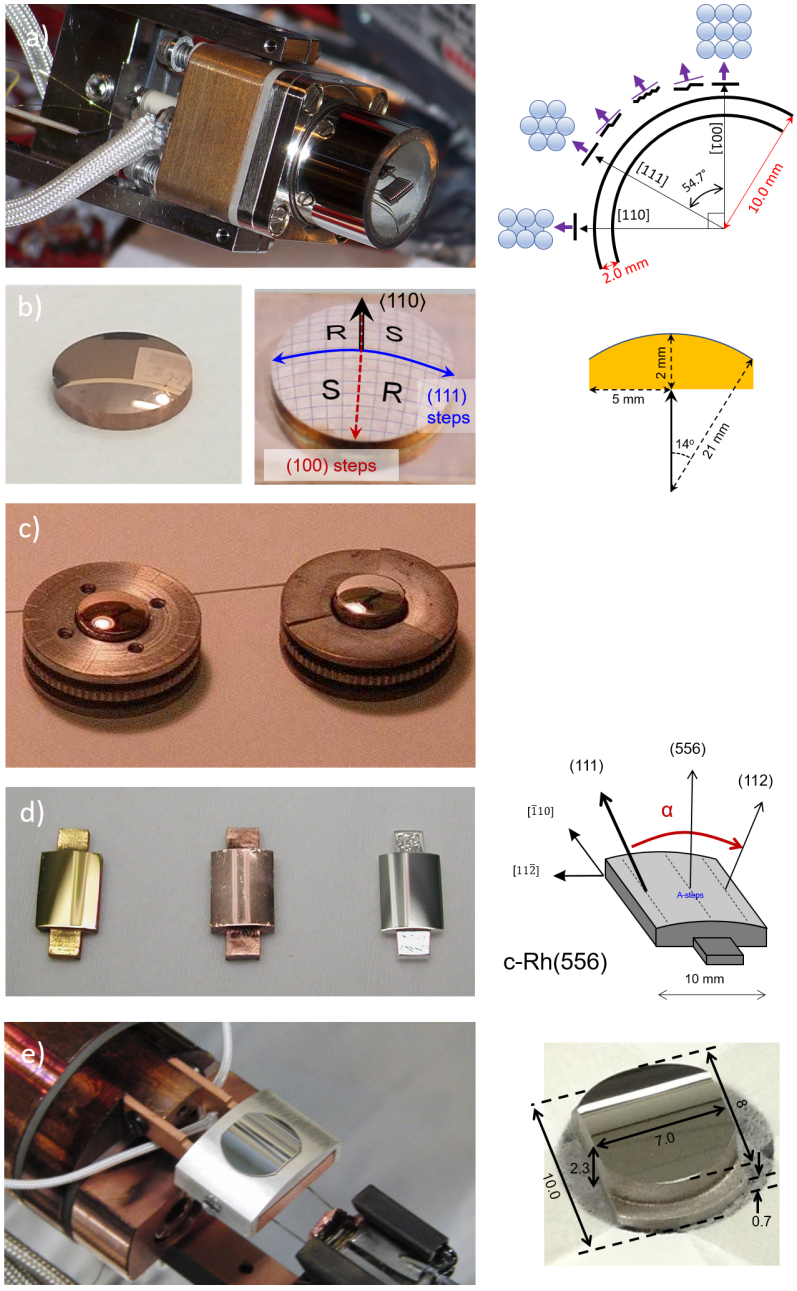

Figure 2.5: Photographs and schematics illustrating more recently used curved single crystals. a) A full Ni cylinder (own work). b) Dome-shaped Cu single crystal (courtesy of prof. dr. Andrew Gellman). c) Dome-shaped Cu and Ag crystals in sample holders (courtesy of prof. dr. Qiu). d) Partial cylinders of Au, Cu and Ag, and schematic drawing of a cylindrical section of a Rh single crystal (courtesy of prof. dr. Ortega). e) Partial Ag cylinder on a manipulator (left), and by itself (own work).

and 1990's. The only more recent example from studies of the Juurlink group is shown in figure 2.5a). Full cylindrical crystals are, as shown in a), bulky. This sample was 20.0 mm in diameter with a 2.0 mm wall thickness. The sample was 14 mm long and oriented along [1$\bar{1}$0]. The shape and externally polished surface make full (hollow) cylinders complicated to connect the sample tightly to a manipulator. The size and weight of full cylinders far exceeds that of typical flat single crystals, increasing demands on power supplies to heat the sample, sputter gun foci, and so on. One also needs to worry about temperature gradients in such large crystals, especially when the cylinder is connected on one side to a cryostat.

Along the cylindrical surface, each surface structure is repeated four times along the curved surface. It allows to check for reproducibility and offers identical surfaces from the same single crystal boule if a part of the polished area is damaged. We know of only the Ni cylindrical crystal to have been used in recent years in surface science studies. We have also produced a Pt sample with the same rotational axis direction, but only used the former in experiments to initiate the combination of curved surfaces with supersonic molecular beam techniques.

Minimizing differences with flat single crystal discs, the most commonly used crystal shape for curved crystals is a section of a cylindrical surface with a flat base. It presents a range of surface structures that depends on its size, the angle of curvature and the rotational axis. The sample size is generally comparable to that of the typical flat disk. Combining differently oriented curved crystals of the same material instead of a full cylinder or dome can be useful and offsets a part of the limitations in surface structure range.[49, 50, 52] Photographs of sections of cylinders are shown in figure 2.5d) and e). The first three crystals of coinage metals used by Ortega in figure 2.5d), curve over a 10 mm width and have extensions in the direction of curvature allowing for easy attachment of the crystal to a sample holder. Whereas these crystals had a low Miller index apex, the schematic illustration in figure 2.5d) shows how a recently used Rh sample has a high Miller index apex, yielding a large range of surface structures passing through the (111) plane. One of our own samples, i.e. a Ag partial cylinder with a (001) apex, is shown in figure 2.5e). Our samples are of similar size as those used by Ortega *et al.*, but have an extended base in the opposite direction. The left photograph shows how our crystals may be held by a cap made of the same material as the crystal and are gently pressed onto a base connecting the crystal to a cryostat.

2.5. NOTATION FOR CURVED CRYSTALS

Curved crystal surfaces were at first predominantly used in either spherical or dome shapes. A standard succinct notation that reflects shapes and surface structural ranges has not yet appeared in the literature. Hence, we suggest a standard notation

that inherently defines the range of surface structures for the most common crystal shapes used nowadays.

For dome shaped crystals it suffices to indicate the apex structure and the angle of curvature. Figure 2.3a-d) showed top views of surface structures near the apex of such domes. As an example of the proposed description, *d*-Cu(111)-90° indicates a dome (*d*) curving 90° in all directions from the apex, i.e. corresponding to a half sphere with (111) at the apex. As the (110) and (001) planes are 35.3° and 54.7° from (111), respectively, all ideal bulk truncated surface structures are well within the range of this surface. A dome with an angle of 55° from the apex would already suffice. Examples of dome shaped crystals with low and high Miller indices at the apex are *d*-Cu(111)-11° and *d*-Cu(432)-19° employed by Gellman and Sykes.[53]

Full cylinders were used by, e.g. Woodruff and coworkers [35–39], Imbihl and coworkers [5, 40–43], and more recently by Juurlink and coworkers [54, 55]. A notation including the rotational axis gives sufficient information to define the entire surface. For the Ni and Cu cylinders used by Woodruff we suggest notations of *cyl*-Cu[110] and *cyl*-Ni[110].

For partial cylinders, we have to specify the apex, direction of curvature, and the curvature's included angle. For example, *c*-Pt(111)[1$\bar{1}$0]-31° indicates a curved Pt crystal with the (111) plane at the apex, curving 31° around a rotational axis of [1$\bar{1}$0], i.e. 15.5° to either side of (111). The information included in this notation implies that A- and B-side steps will be found on the two sides of the crystal, with the (111) terrace widths decreasing from the apex to 4-5 atom rows at the sides.

For uncommon crystal shapes, a similar style could be used. For example for a conical crystal, *con*-M(*hkl*)X°could indicate (*hkl*) as the pointy apex of the cone and X the included angle.

2.6. CONSIDERATIONS REGARDING EXPERIMENTAL APPLICATIONS OF CURVED CRYSTALS

Curved samples may be created, e.g., by spark erosion, with subsequent hand-polishing. While various research groups still use this approach successfully, metal curved single crystal samples can, nowadays, also be purchased from, e.g., Surface Preparation Laboratories (Zaandam, the Netherlands). This company has developed an automated polishing technique with a high level of control over the pressure applied to the rotating crystal when slowly polishing it over a cloth that also rotates and translates.

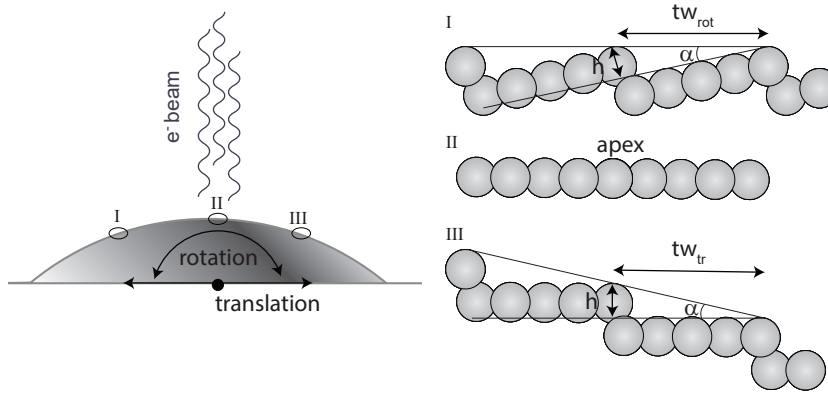

Figure 2.6: Illustration of the way in which stepped surfaces are exposed in the case of rotating or translating the curved crystal from the low-Miller index plane. If the apex of the crystal (II) is aligned normal to, e.g. an incoming electron beam, surface structures at the sides of the crystal can be exposed by either rotating the crystal along its axis, or translating away from the apex. In the case of rotation (I), stepped surfaces are exposed with their surface normal along the probing beam. In the case of translation (III), stepped surfaces are exposed with the low-Miller index terrace normal along the probing beam.

2.6.1. TERRACE WIDTHS AND STEP DENSITIES ON CURVED SURFACES

Some level of spatial resolution is required to make use of a curved crystal's potential and correlate physical properties or chemical reactivities to surface structure. A thorough understanding of where on the curved crystal which structures appear is thus essential. Surface structures along curved cylindrical crystals depend on the rotation axis and the miscut angle α from the low Miller index surface. Generally, either consecutive small fractions of the surface are probed and exposed to molecules, photons, or electrons in an experiment, or a signal coming from a small part of the surface is detected while the entire surface is treated (or exposed) in the same manner. In few experimental techniques, the entire surface is exposed and probed at once. For example, planar laser-induced fluorescence (PLIF) visualizes product formation above the entire surface while the crystal is uniformly exposed to reactant gases. Under most circumstances, however, moving the crystal's surface relative to some beam exposing or probing the surface is required. This may either be achieved by rotating or translating the crystal on an x, y, z, Θ-manipulator. Figure 2.6 provides illustrations to introduce some general considerations regarding experimental application of curved surfaces.

If the different parts of the curved crystal are probed by rotation, the probe is always directed to the surface along the surface normal. The observed terrace width from one step to the next in this case corresponds to:

$$tw_{rot} = \frac{h}{\sin\alpha} \tag{2.1}$$

where h is the step height or distance between low Miller index terraces.The parameters tw_{rot}, α, and h are illustrated in panel I of figure 2.6 for a monoatomic step. In the case of consistent step doubling, h is simply twice the layer-to-layer stacking height and the average tw becomes twice as large. For the low-Miller index surfaces displayed in figure 2.2, values for monoatomic step heights h as a function of the lattice unit cell height a (c for *hcp* lattices) are given in table 2.1. The step density, sd, for the case of sample rotation is

$$sd_{rot} = \frac{1}{tw_{rot}} \tag{2.2}$$

For accessing different parts of the curved crystal by translation instead of rotation, it is useful to convert the angle α to a translational distance, d.

$$d = \sin\alpha \cdot r \tag{2.3}$$

Here, r is the radius of the curved crystal. Surfaces are - in the case of a low Miller index apex, now always probed or exposed along the low Miller index terrace normal, i.e. not the macroscopic surface normal. The observed terrace width can be described by

$$tw_{tr} = \frac{h}{\tan\alpha} = \frac{h}{\tan\left(\sin^{-1}\left(d/r\right)\right)} \tag{2.4}$$

The step density (sd) is still given as

$$sd_{tr} = \frac{1}{tw_{tr}} \tag{2.5}$$

The parameters tw_{tr}, α, and h for translation are also shown in panel III of figure 2.6. Note that translating the crystal may lead to minor changes in signal intensity during experiments due to varying distance of the probed surface to the detector.

Figure 2.7 visualizes the consequences with respect to the probed terrace width and step density for the four atomically flat planes of *fcc*, *bcc* and *hcp* unit cells. The left and right axes present terrace widths and step densities normalized for the unit cell parameter, a (c for *hcp*), versus the angle from a low Miller index apex. The latter is also converted to a linear translation from the apex, normalized for the radius of curvature.
Normalized terrace widths and step densities versus angle from the low-Miller index apex (bottom axis) are given in solid lines. For cases where the curved surfaces is translated, dashed lines give normalized terrace widths and step densities as they vary with distance from the apex (top axis). Values on the top axis must be multiplied

terrace plane	monoatomic step height (h)	step type	step atom spacing (g)	spot splitting to row spacing (ss/rs)
fcc(111)	$\frac{1}{\sqrt{3}} \cdot a$	A / B	$\frac{1}{\sqrt{2}} \cdot a$	$\frac{\sqrt{3}}{\sqrt{2}} \cdot \sin\alpha$
		fully kinked	$\frac{\sqrt{3}}{\sqrt{2}} \cdot a$	$\frac{3}{\sqrt{2}} \cdot \sin\alpha$
fcc(001)	$\frac{1}{2} \cdot a$	A'	$\frac{1}{\sqrt{2}} \cdot a$	$\sqrt{2} \cdot \sin\alpha$
		fully kinked	a	$2 \cdot \sin\alpha$
bcc(110))	$\frac{1}{\sqrt{2}} \cdot a$	{211}	$\frac{\sqrt{3}}{2} \cdot a$	$\frac{\sqrt{3}}{\sqrt{2}} \cdot \sin\alpha$
		{111} / fully kinked	$\sqrt{2} \cdot a$	$2 \cdot \sin\alpha$
hcp(0001)	$\frac{1}{2} \cdot c$	A-B	$\frac{\sqrt{3}}{\sqrt{8}} \cdot c$	$\frac{3}{\sqrt{2}} \cdot \sin\alpha$
		fully kinked	$\frac{\sqrt{3}}{\sqrt{2}} \cdot c$	$\sqrt{6} \cdot \sin\alpha$

Table 2.1: Flat low-Miller index surfaces in the *fcc*, *bcc*, and *hcp* crystal lattices, and important parameters for vicinal surfaces. The step height (h) is defined as the stacking height between planes along the same orientation, and listed as a function of the crystal lattice parameter a (c for hcp) as indicated in figure 2.2. For all planes, close packed and fully kinked step types are given. The parameter g gives the separation of equivalent step atoms along the step edge of each type. Lastly, according to equation 2.6, the previous parameters can be used to determine the *spot splitting to row spacing* ratio observed in LEED patterns of vicinal surfaces, as a function of the angle α between the terrace normal and the surface normal.

by the radius of curvature of a sample, to obtain values with a unit, e.g. mm. Normalized terrace widths need to be multiplied by the lattice parameter a (c for *hcp*) to obtain values with a unit, e.g. nm, or Å. Normalized step densities need to be divided by the lattice parameter a (c for *hcp*) to obtain values with a unit, e.g. nm^{-1}, or $Å^{-1}$.

2.6.2. DIFFRACTION OF REGULARLY STEPPED SURFACES ALONG THE CURVATURE

The average step density at different position along the surface of a curved crystal can be examined by LEED. The well-known LEED patterns for low Miller index surfaces are easily identified along a curved crystal surface. When probing increasingly stepped surfaces, the 'superlattice' of steps arrays causes an additional diffraction criterion, resulting in spot splitting. [30, 56] For a low Miller apex, the specular spot in the LEED pattern overlaps with the (0,0) spot of the low Miller index plane and is - in most common equipment - hidden behind the electron gun. When subsequently translating the crystal, causing visible spots to split, the specular spot also moves and

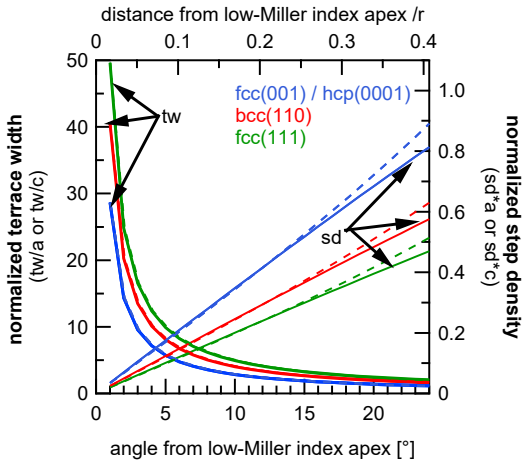

Figure 2.7: Change of normalized mean terrace width and normalized step density when rotating (bottom axis, solid lines) or translating (top axis, dashed lines) a curved crystal with a low-Miller index apex. Behavior is shown for fcc(111) (*green*), bcc(110) (*red*), and the identical fcc(001) and hcp(0001) (*blue*). The *tw* and *sd* are normalized for the unit cell parameter, *a* (*c*), of the respective material. The distance from apex (top axis) is normalized to the radius of curvature, *r*.

may becomes visible on the LEED screen. It is displaced by the miscut angle α, i.e. the angle between the overall surface normal and the low-Miller index terrace normal. When rotating the sample's surface at the focus of the LEED optics instead of translating, the entire observed diffraction pattern rotates while spot splitting varies. Here, the specular spot on the LEED screen also remains hidden behind the electron gun.

The splitting increases linearly with narrowing of the terraces. The ratio of the distance between split spots, *ss*, and the spacing between rows of split spots, *rs*, in LEED patterns of stepped surfaces is the inverse of the ratio between the average terrace width and spacing of equivalent atoms, *g*, along the step edge:

$$\frac{ss}{rs} = \frac{1}{tw_{rot}} \cdot \frac{g}{1} \tag{2.6}$$

Van Hove and Somorjai calculated these ratios for a limited number of stepped *fcc* surface structures.[57] Here, with the universal formula in equation 2.6, it becomes straightforward to predict spot splitting to row spacing ratios for any type of regularly stepped surface and for all lattice structures. Table 2.1 lists spot splitting to row spacing ratios for the types of stepped surfaces discussed before. They only dependent on the surface angle from the low-Miller index plane and the lattice constant *a* (or *c*) of the material.

2.7. RECENT ADVANCES

In the last two decades, advances in the polishing of curved crystals and adaptation of various surface science techniques to accommodate these samples have resulted in a new wave of curved crystal surface science studies. Of particular importance is the application of STM. The technique has proven extremely useful in studying the wide range of vicinals featured on curved crystals. It has, in many cases, revealed how subtle structural changes influence the physical properties or chemical reactivity. Research employing curved samples has primarily been carried forward by the groups of Ortega and coworkers at the DIPC in San Sebastian (Spain) and their recent collaboration with Lundgren and coworkers at Lund University (Sweden), a collaboration of the research groups of Sykes at Tufts University (USA) and Gellman at Carnegie Mellon (USA), and our own group at Leiden University (the Netherlands). Near the turn of the millennium, a series of papers were published by the groups of Bader (Argonne National Labs) at Qiu (UC Berkeley) on properties of overlayers deposited on curved single crystal samples. We take the order of first discussing what has been learned on the structure of clean transition metal curved surfaces in recent years prior to discussing adsorption and desorption of molecules, chemical reactions, as well as studies of overlayers grown on top of curved samples.

2.7.1. STRUCTURE AND ELECTRONIC STATES OF CLEAN METAL SURFACES

NOBLE METALS

The first thorough STM study of a clean and uncovered curved crystal surface was published in 2008 by the group of Ortega (San Sebastian, Spain).[58] There, a Au crystal was used to study faceting of (111) vicinals. A hill-and-valley structure was observed over a range of 6 °, i.e. 4 - 10 ° from the (111) apex. Outside this range, the surface showed atomically smooth terraces with single atom high steps. Faceting of the stepped surfaces into a hill-and-valley structure was observed. This structure comprised of two specific, experimentally determined terrace widths, d_w (wider terraces with herringbone reconstruction) and d_n (narrow terraces without herringbone reconstruction). The smoothly variable miscut angle made it possible to define the limits of faceting on the stepped Au surfaces. Furthermore, being able to compare the two sides of the crystal revealed differences in faceting behavior for the A- and B-type steps, i.e. a difference in the sequence of the d_w and d_n terraces.[59]

The combination of STM with angle-resolved photoemission spectroscopy (ARPES) yielded detailed and unprecedented insights into the origin of faceting. Synchrotron radiation for ARPES ensured a narrow energy profile as well as a small beam size on the curved surface (100 μm), minimizing convolution across different surface structures. The two terrace widths, caused by band splitting into a low and high energy

state, induce band folding and opening of energy gaps at the Fermi level. It was found that the two phases are favored on the vicinal surfaces because they lower the electronic surface energy (d_w) and improve faceting kinetics (d_n). The two phases differ in elastic interactions due to varying step stiffness, step dipole, and terrace stress. The different behavior on the two sides of the crystal were attributed to the respective step arrangement at A or B-type steps. These cause a preference for defined mixing of phases (A-type) or partial phase separation (B-type). For A-type steps, the regular arrangement of d_w and d_n phases gives a defined superlattice, resulting in coherent electronic coupling between the phases.

Realizing the possibilities of curved crystals in examining structural and electronic effects, a series of publications using curved noble metal crystals followed. Continuing their previous work on the interplay between electronic structure of noble metals and their surface structures, Ortega and coworkers utilized the step arrays on curved crystals as tuneable superlattices. They used the regularly stepped surfaces on the curved crystals to introduce periodic potential barriers to the free-electron-like surface bands of noble metals, causing the electrons to scatter off the steps. Comparing three partial cylindrical slices of noble metal surfaces, oriented around (111) and shown in figure 2.5d), namely *c*-Au(111)[1$\bar{1}$0]-30°, *c*-Ag(111)[1$\bar{1}$0]-30°, and *c*-Cu(111)[1$\bar{1}$0]-30° crystals,[60] the authors found terrace confinement effects of surface electrons in each case. The effect increases in strength from Ag to Cu to Au vicinals. The previously observed faceting for Au and structural instabilities around $\frac{1}{2}\lambda_F$ for Cu were detected, but no structural instability was observed for Ag. From ARPES data, the previously unknown effective barrier strengths of monoatomic steps on (111) terraces could be determined for all three metals. Later, they showed that such steps can act both as repulsive and transmissive barriers for surface electrons. The nature of the barrier does not depend on the spacing between steps, but on the order in step arrays which can cause coherence. [61] The (dis)order either leads to coherent 2D surface states or 1D quantum wells.

Beyond the regularity of close-packed step arrays and electronic effects, the (mostly) smoothly varying step density on curved crystal surfaces of noble metals makes them a prime tool to investigate step-step interactions. These interactions consist of elastic repulsion (dipole effects) and entropic repulsion (related to step stiffness). A bulk Ag curved crystal (*c*-Ag(645)[11$\bar{2}$]-24°), featuring (111) vicinals with fully-kinked step edges, was used to test the generalized Wigner-surmise.[62] The order parameter, ρ, which relates to the relative strengths of entropic and elastic step interactions, increases linearly with step density. This finding indicates a changing ratio of elastic-to-entropic interaction which had not previously been considered within the terrace-step-kink (TSK) model.

Studied in much less detail, the surfaces of two similar curved Ag samples were also used in our group. [50, 63] One is shown in figure 2.5e). Both crystal's surfaces were

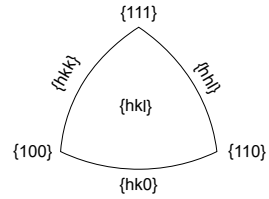

Figure 2.8: Schematic representation of the "stereographic triangle" of surfaces contained between the high-symmetry *fcc* planes, (001), (110), and (111).

initially studied using LEED only. Whereas a *c*-Ag(111)[1$\bar{1}$0]-31° crystal was easily cleaned and LEED results showed no indications of unexpected surface irregularities, *c*-Ag(001)[1$\bar{1}$0]-31° proved to be difficult to handle. Likely a single or few cleaning cycles involving sputtering at normal incidence damaged the surface consisting mostly of (001) terraces to an extent that it took more than 6 months to 'repair'. Several hundred cleaning cycles of mild Ar^+ sputtering at 45 ° incidence, interspersed with mild annealing, ultimately recovered the surface. Spot splitting-to-row spacing ratios in the square LEED patterns were found to be as expected along most of the curved surface.

STM studies of Cu surfaces with both atomically straight and kinked steps was also an integral part of the work on dome-shaped Cu crystals by Gellman et al. Six Cu crystals were polished in-house from disk-shaped samples to cover the entire *(S)*-chiral stereographic triangle of *fcc*, shown in figure 2.8.[51] One of these crystals is shown in figure 2.5b). These so called 'surface structure spread single crystals', *d*-Cu(111)-11°, *d*-Cu(100)-10°, *d*-Cu(110)-11°, *d*-Cu(432)-19°, *d*-Cu(821)-14°, and *d*-Cu(861)-10° allowed the characterisation of structures at all possible surface orientations. Surface structures were reported to predominantly follow the expected bulk-terminations with local fluctuations at specific orientations.

PT-GROUP METALS

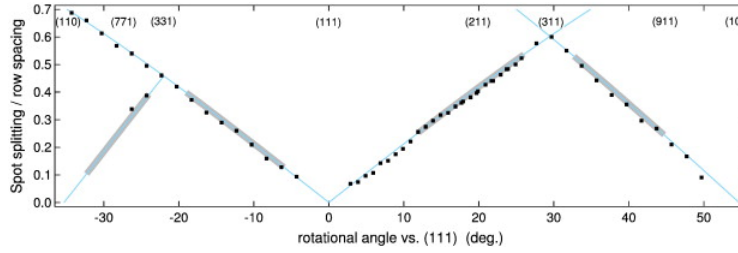

Figure 2.9: Spot splitting-to-row spacing analysis for a *cyl*-Ni[110] crystal. Data are shown as dots. The ideal expected values are shown as solid lines. Areas where streaking was observed are indicated by grey bars. Reprinted from [55], Copyright (2013), with permission from Elsevier.

A 12 mm diameter cylindrical nickel sample, *cyl*-Ni[110], has been used by Woodruff

and coworkers in the 1980's.[36] The study reported on cleanliness and oxidation of the surface, but the study lacked diffraction techniques to verify surface order. More recently, a 20 mm diameter cylindrical nickel crystal with the same orientation was used in our group.[54, 55] It is shown in figure 2.5a). The cleaned surface structure of this *cyl*-Ni[110] was studied by LEED.[55] Using a multichannel plate (MCP)-based LEED allowed for use of a very small electron beam (0.3 mm diameter), thus improving spatial resolution in comparison to the more common reverse view LEED with a hemispherical fluorescent screen. However, it complicated the interpretation of the diffraction patterns. They are distorted from the usual direct visualization of the Ewald sphere as a consequence of the MCP being flat instead of hemispherical. LEED patterns of surfaces with broad (111), (110) and (100) terraces appeared as expected as well as highly stepped surfaces. Where patterns appeared as expected, a step height analysis based on variation of the incident electron energy confirmed monoatomic high steps. LEED patterns showed significant streaking in between the more crisp patterns. The streaking was attributed to increased disorder and partial reconstruction of the surface. The spot splitting-to-row spacing analysis shown as a Bauer-plot is reproduced in figure 2.9. It visualizes that the cylindrical crystal over the probed 90° consists to some extent of expected monoatomic step arrays (B-type step in between the (331) and (111), A-type step in between (111) and (311), and A'-type step in between (311) and (100) surfaces), but likely also shows lower degrees of ordering and reconstruction over significant fractions of the circumference. Surface quality was suggested to relate to the exact cleaning procedures and a single cleaning procedure that does not induce faceting or other types of reconstruction on some parts of the included 90° curvature may not exist.

Several years later, a more detailed structural study was performed on a cylindrical section of a Ni single crystal, i.e. *c*-Ni(111)[1$\bar{1}$0]-27.5°.[64] Step-type dependent step-doubling was shown to result from strong elastic interactions between steps. A combination of STM and LEED (300 μm spot size of the electron beam) revealed the progressive transition from monoatomic steps to double steps (and consequently double terrace lengths) for A-type steps. Only monoatomic height steps occurred for B-type steps separating (111) terraces. The onset of the transition to doubling of A-type steps was found to be temperature dependent. The B side maintained consistently monoatomic steps over the probed temperature range, but saw a 10 % decrease of the spot splitting to row spacing at temperatures above 450 K as compared to room temperature. It was suggested to indicate an increase in entropic repulsion between steps. Varying the miscut angle on the curved crystals, as well as the surface temperature allowed the authors to construct an (α,T)-phase diagram for step doubling on Ni(111) vicinal surfaces.

Several studies have used curved Pt surfaces. These follow the earlier studies of a hand-polished *c*-Pt(111)[1$\bar{1}$0] sample used by Comsa and coworkers[33], who re-

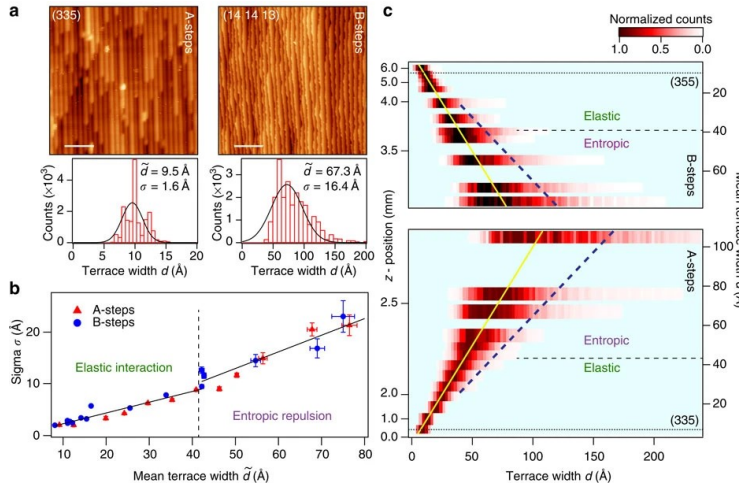

Figure 2.10: STM analysis of a *c*-Pt(111)[1$\bar{1}$0]-30° crystal, revealing changes in the interplay of elastic and entropic interactions in step arrays with varying terrace width. a) Two examples of STM images of surfaces with A- and B- type steps and the associated distributions of terrace widths including Gaussian lineshape fits and fit parameters (average terrace width, $\tilde{d}$, and standard deviation, σ) . b) Variation of standard deviation with mean average terrace width over a range of ~4 to 30 atom rows. c) Image plot of terrace width distributions spanning the curvature. Figure reprinted from reference[65], under Creactive Commons CC BY license. Copyright 2015, The authors.

ported that a LEED study showed the expected diffraction pattern with spot splitting smoothly increasing from the (111) apex up to the ~7 atom row wide terraces at the edges of the crystal, and a *cyl*-Pt[001] by Ertl and coworkers who reported faceting in between (100) and (110) planes as illustrated in figure 2.1.[5]

For a curved Pt(111) crystal with close-packed (A- and B-type) steps, i.e. *c*-Pt(111)[1$\bar{1}$0]-30°, a step density dependent transition from a regime dominated by elastic interactions to a regime with predominantly entropic repulsion was found by Ortega and coworkers.[65] Figure 2.10 illustrates results. Arrays of monoatomic steps were reported for both sides of the crystal with terrace width distribution from 4 to ~ 40 terrace atom rows that were fitted by Gaussian lines shapes. The plotted relation between the distribution's width and the average terrace width shows two linear regimes separated by a kink near 40 Å. It was argued to result from the predominant type of step-step interaction.

We very recently used a similar crystal, but with highly kinked steps, i.e. *c*-Pt(111)[11$\bar{2}$]-31°.[49] The structural analysis of this crystal is presented in chapter 3.

The surface of a *c*-Pd(111)[1$\bar{1}$0]-30° crystal has been studied as part of a broader study on the structure dependence in chemical activity toward CO oxidation.[66] The surface structure of the bare metal was beforehand investigated by STM, LEED, and XRD and showed no deviations from expected surface structures. The maxima in terrace

width distributions obtained from STM images consistently agreed with the value for mean terrace widths. In contrast to the study on *c*-Pt(111)[1$\bar{1}$0]-30°, no transition between regimes of dominant elastic and dominant entropic step-step interactions, was observed. This difference was attributed to stronger elastic repulsion between A- and B-type steps on Pd than on Pt(111) vicinals.

OTHER TRANSITION METALS

A *c*-Rh(111)[1$\bar{1}$0]-32°, employed in a CO oxidation study by Garcia-Martinez *et al.*, was investigated with regards to its surface structure by LEED.[67] Spot-splitting increases linearly with distance from (111), for both A- and B-type steps. No indications of deviations from the expected stepped surface structures were identified. Additionally, the XPS fingerprints of bulk, terrace and step species were identified. The XPS signal from the terraces decreases towards the sides of the crystal, which was attributed to tensile stress from the neighboring steps at narrow terraces.

A *c*-Co(0001)[1$\bar{1}$00]-31°crystal was briefly studied in our group by LEED only. The phase transition from *hcp* to *fcc* is a worry in cleaning Co single crystals. During surface preparation, temperatures remained well below the onset temperatures for the phase transition tabulated for this metal.[68] Regardless, LEED patterns showed a hexagonal pattern with some spot splitting that suggested massive surface reconstruction. However, the direction of spot splitting was inconsistent with the expected direction for kinked steps, leaning strongly toward the direction expected for close-packed steps. Spot splitting-to-row spacing ratios also did not vary as expected with distance from the apex. They even remained constant while translating the crystal relative to LEED electron beam. These results may suggest massive surface reconstructions, but are inconclusive and remain unpublished.

2.7.2. ADSORPTION AND DESORPTION FROM CURVED SURFACES

To study surface structure dependencies of (non-)dissociative adsorption and (recombinative) desorption of molecules from surfaces, several techniques have been applied in recent years. While some of these required adaptations to provide required spatial resolution, e.g. reflection-absorption infrared spectroscopy (RAIRS) and temperature programmed desorption (TPD), others, e.g. XPS and STM, may not.

TEMPERATURE PROGRAMMED DESORPTION

To use thermal desorption as a technique in studies of surface structure dependencies with curved crystals, one can deposit the species of interest onto a small (narrow) area of a curved crystal surface where structural variation is small or negligible, and subsequently monitor desorption. Here, imposing spatial resolution in the detection

is not required, but may help to improve the signal-to-noise ratio or other complications, e.g. slopes in background signals. It does require a dosing technique, e.g. a (supersonic) molecular beam that is appropriately skimmed prior to impact on a well-defined part of the crystal's curved surface. The other straightforward option is to monitor the desorption from a small area after exposing the entire surface, e.g. by a differentially pumped QMS with an orifice that strongly limits the acceptance of molecules desorbing from the curved surface. In Leiden, we have applied both options.

In a first proof-of-principle study using a *cyl*-Ni[110] crystal, a rectangularly skimmed supersonic molecular beam deposited deuterium atoms by dissociation of D_2 onto the surface.[54] The footprint of the beam was either 1.0 or 0.4 mm high and 5.2 mm wide along the [110] rotational axis. From the deposition position, the crystal was rotated by 180° along the axial [110] direction so that the exposed area faced the 1.0 mm high and 6.0 mm wide opening into a differentially pumped QMS housing. Successive experiments dosing and desorbing D_2 showed that the characteristic double-peaked feature of hydrogen desorption from Ni(111) could clearly be found along the surface, as well as the progressive changes in the TPD spectrum with changes in the probed surface structure. The incorporation of (100) steps separating (111) terraces led to a decrease in the intensity of the lower peak and an upward shift in the desorption temperature of the highest peak, suggesting that these A-type steps bind atomic deuterium stronger than (111) terraces. A peak shift of ~10 K was found for rotation of the crystal over 20°, i.e. from an area exposing very large (111) terraces to a surface with ~3 atom row wide (111) terraces.

Two more detailed studies using H_2O and two *c*-Ag single crystals were conducted without dosing from a supersonic molecular beam. Crystals were exposed to (deuterated) water from an effusive capillary array-based source. TPD spectra obtained using a rectangular orifice at 1 mm from the crystal surface showed that even smaller shifts could be accurately traced and interpreted. [50, 63] Results are presented in chapter 6 of this thesis.

REFLECTION ABSORPTION INFRARED SPECTROSCOPY

To study molecular adsorbates or fragments thereof, RAIRS is a powerful technique. It is most easily performed with fixed IR incident and reflected beam paths. A curved single crystal surface must then be applied so that the crystal can be rotated along its curved surface, with the IR beam, shaped to a narrow stripe, reflecting off the surface at the same angle regardless of the probed surface structure. While this may be the optimal approach for cylindrical samples, we have taken a different approach for partially curved crystals. Figure 2.11 illustrates in three views how we counter the varying deflection angle of the IR beam when translating a curved crystal's surface along the IR beam's focal point using an internally Au-coated curved mirror.[69] In

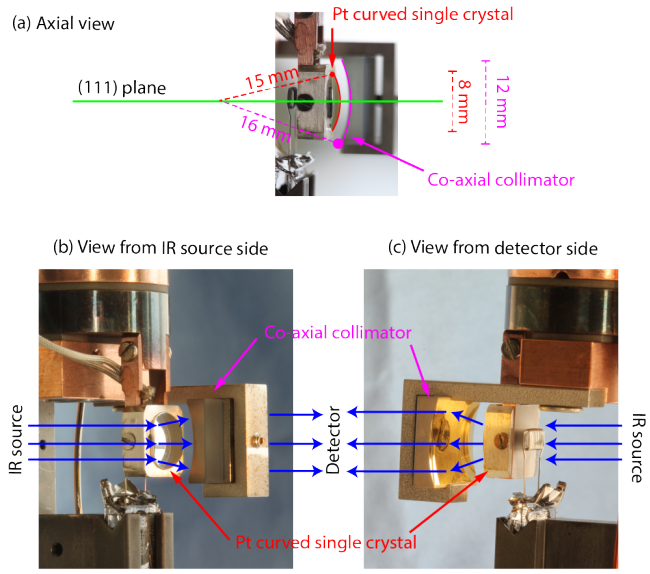

Figure 2.11: Views from different angles of the curved crystal and internally curved Au coated mirror. Both are individually attached to a cryostat. The internally coated Au mirror fixes the position of the exiting IR beam in RAIRS experiments and was used to probe CO adsorption to a c-Pt(111)[1$\bar{1}$0] curved crystal. A similar figure appears in reference [69].

this proof-of-principle study, we probed the adsorption and desorption of CO with c-Pt(111)[1$\bar{1}$0]-31° while translating the crystal up and down relative to the fixed IR focus in the UHV chamber. IR light reflected from the sample is deflected upward or downward depending on the crystal's vertical position. When the crystal is translated downward and the IR focus is above the apex, the reflected beam moves upward and vice versa. This deflection is countered by the sideways off-set Au-coated mirror. Besides correcting the deflection, it acts as a collimator to the diverging IR beam. While spatial resolution is limited and depends, *a.o.*, on the aperture size behind the IR source in the FTIR spectrometer, we showed that we could track the shifts and intensity variations for CO adsorbed at various coverages on the entire range of surface structures present on the curved samples. IR absorption by both on-top and bridge adsorption positions could be tracked quite accurately, illustrating how CO adsorbed to step sites act predominantly as defects to the exitons at intermediate step densities. As a consequence, the narrow line width that dominates the spectra at both high and low step densities, broadened at intermediate step densities. Bridge adsorption was, contrary to previous reports, not found on the A-type stepped surfaces, while it was clearly present on B-type stepped surfaces. As an XPS study on CO adsorption to a similar curved Pt sample confirmed the earlier assignments of different adsorption sites found by flat single crystals[65] (see below), a simple explanation may be that IR spectra of the curved surface in our study (ref. [69]) were accidentally reversed.

X-RAY PHOTOELECTRON SPECTROSCOPY

High spatial resolution on curved crystals can easily be be achieved when synchrotron radiation is employed. This approach was used by Ortega and coworkers, e.g. during experiments studying CO adsorption and oxidation at near-ambient pressures. On a *c*-Pt(111)[1$\bar{1}$0]-30° sample, XPS was used to demonstrate the preference for initial CO adsorption at steps.[65] Differences between step types were exposed by comparing the two sides of the crystal. CO adsorbs only at on-top positions at the upper edge of B-type steps and in both on-top and bridge positions at A-type steps. Terrace adsorption occurs after step edges are fully saturated with CO.

A similar study was also performed for *c*-Rh(111)[1$\bar{1}$0]-32°. CO adsorption occurred at the on-top sites of steps first, followed by terrace on-top sites. Only at higher coverages were bridge sites at steps and hollow sites on terraces occupied.[67]

As an alternative to synchrotron radiation, laboratory XPS equipment can be modified to improve spatial resolution. For example, a special XPS probe was used by Gellman and coworkers to achieve spatial resolution of less than 0.2° angular spread on dome-shaped sample to study, e.g. oxygen uptake during surface oxidation [53] and the activity of decomposition of aspartic and tartaric acid on Cu surfaces.[70, 71] The results will be discussed in section 2.7.3.

SCANNING TUNNELING MICROSCOPY

Clearly, STM can be applied to study adsorption of molecules on stepped surfaces. However, very few studies have appeared so far. STM studies of the surface oxidation of Cu and Ag surface are postponed to the following section, as well as studies of the adsorption and decomposition of chiral molecules on chiral Cu surfaces (discussed in section 2.7.3).

2.7.3. CHEMICAL REACTIONS AT CURVED SURFACES

SURFACE OXIDATION

A dome-shaped Cu(111) crystal was employed to study surface oxidation on Cu(111) and all vicinals by Gellman ad Sykes.[53] Oxidation in the topmost layer of (111) terraces, characterized as Cu_2O, was found to grow in triangular shapes given by the three possible directions of A-type steps. A subsequent oxidation layer, originating from Cu atoms expelled from the topmost layer, grew on top of the triangular oxide domains, but this second layer had itself no defined shape. At steps, boundaries between the step oxide phase and upper (111) terraces also followed the directions of A-type steps, leading to substantial faceting at B-type and kinked steps, but almost no reconstruction at A-type steps. Overall, the rate of oxidation was found to increase significantly with step density from (111) towards the edges of the crystal. However,

despite the structural differences of oxide phases, the rate depended not on step-type or kink density. XPS was used to determine rates and uptake of oxygen on parts of the dome-shaped crystal. Here, foregoing the use of synchrotron radiation, a special XPS probe was used to achieve spatial resolution of less than 0.2° angular spread on the sample. The potential of these types of crystals for the optimisation of possible structures and compositions of catalyst particles was quickly realised.[72]

The chiral metal surfaces on the *d*-Cu(111)-11° surfaces were recently used as a template for the growth of a chiral metal oxide surface.[73] There, depending on step chirality and predominant step-type, growth of homochiral domains of the "29" Cu oxide could be induced. This oxide features a chiral pore structure. A combined LEED and STM study of the dome-shaped crystal demonstrated direct transfer of chirality from a metal template to an oxide film for the first time. Figure 2.14 shows STM images of oxide structures on surfaces with varying step orientation, as published in the original publication.

A similar study using a curved *c*-Ag(111)[$1\bar{1}0$]-31°crystal has recently been conducted by Killelea and coworkers. Here, the oxidation requires a harsher oxidant as the dissociation probability of molecular O_2 is extremely low on silver. The curved surface was exposed to atomic oxygen created from a hot iridium filament kept in low pressure oxygen background. Progressive oxidation was followed by imaging the typical silver oxide overlayer at 35 K after various exposures at two different surface temperatures. Detailed results are forthcoming.[74]

Oxygen adsorption and dissociation was also studied on a curved platinum surface.[75] Here, the study intended to unravel how A- and B-type steps contribute to the increased sticking probability of O_2 on stepped (111) surfaces compared to the Pt(111).[76] At low incident energy, the sticking probability - as measured by molecular beam methods - was found to scale linearly with step density and did not vary with step type. At higher incident energies, the beneficial effect of step in trapping and dissociation O_2 vanished to a significant extent while a step type dependence appeared. A collaboration with dr. Kurahashi at the National Institute for Materials Science (Tsukuba, Japan) helped determine the origin by state-selecting and orienting impinging O_2 molecules. Here, the curved crystal was replaced by three flat single crystals that spanned the same range of surface structures as present on the curved Pt crystal. Results indicated that, at low incident energy, scattering of steps improves translation energy loss for molecules approaching along the [111] normal of the terraces, trapping the molecules initially into a physisorbed state. At higher kinetic energies, direct adsorption into molecular chemisorbed state becomes possible. The experiments confirmed that this molecular state is characterized by the O=O bond lying parallel to steps and the binding energy varying for the A- and B-type steps.

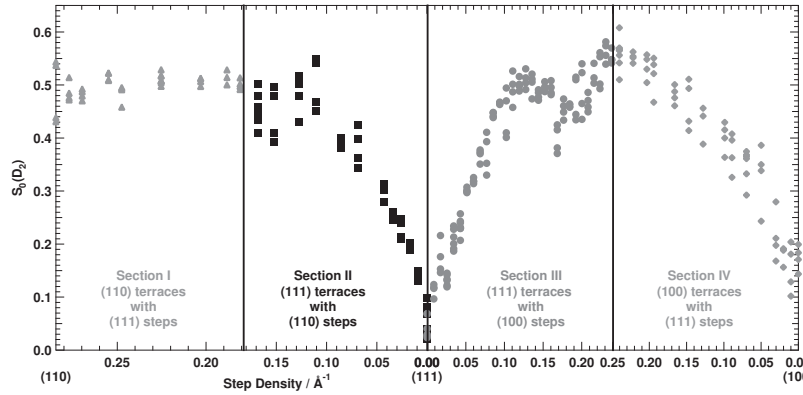

Figure 2.12: Initial dissociation probability, S_0, at 0.82 kJ/mol incident energy for D_2 as measured by the King and Wells technique on *cyl*-Ni[110] with incidence of the beam along the local surface normal.[77] S_0 is determined over a 90° angle, spanning all stepped surface structure from (110) via (111) to (100). Two additional vertical lines indicate the (331) and (311) positions.

HYDROGEN DISSOCIATION AND H-D EXCHANGE

The same supersonic molecular beam technique with a rectangularly skimmed footprint as described to study D_2 desorption from well-defined areas on a *cyl*-Ni[110] crystal (section 2.7.2) was also applied to study the structure and energy dependence of D_2 dissociation on Ni.[54] While the original publication showed various individual King and Wells traces for different surface structures and different incident energies, figure 2.12 shows the results for a low incident energy over the same 90° rotation as used in figure 2.9. The initial sticking probability, S_0, increases linearly over a large step density range vicinal to the (100) and (111) planes. It suggests that the dissociation probability at steps is much higher than at the respective terraces and that the measured reactivity represents a linear combination of both. Noteworthy were the step density independence in section I, i.e. in between the (110) and (331) planes, and the dip in the otherwise linearly increasing dissociation probability in section III, i.e. between (111) and (311). The first observation was taken to imply that slight stretching of the 111 facets making up the (110) plane does not alter the reactivity toward D_2 dissociation. For the second observation, the streaking observed in the same area in LEED patterns was taken to suggest faceting or some other local restructuring that would lower step densities close to (311). This idea was later confirmed by the structural study on the *c*-Ni(111)[1$\bar{1}$0]-27.5°crystal by the San Sebastian group who showed that the A-type step shows step doubling (i.e. region III), but not the B-type (i.e. region II). [64]

Dissociation of D_2 on steps of Pt was studied in a similar fashion, but with significantly improved spatial resolution and using a *c*-Pt(111)[1$\bar{1}$0]-31°crystal.[78] This first study focused on the mechanism of dissociation, which had been debated for ap-

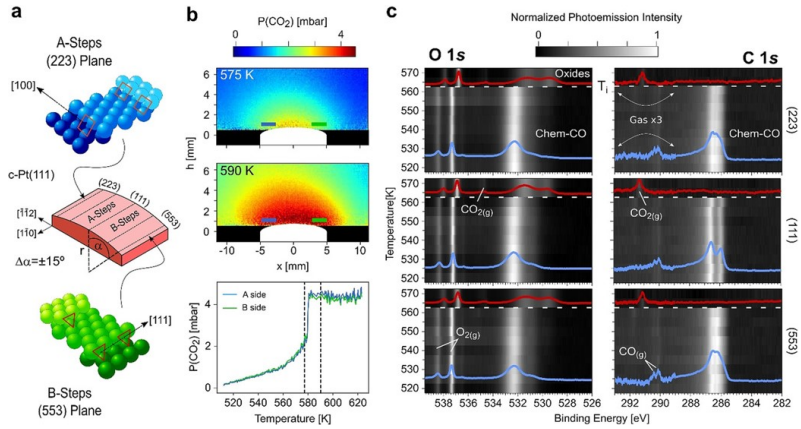

Figure 2.13: PLIF and XPS study of CO oxidation under near-ambient pressure on the surface of a *c*-Pt(111)[1$\bar{1}$0]-30° crystal. a) Representation of A- and B-type steps appearing on different sides of the curved crystal. b) Two images of planar laser-induced fluorescence of CO_2 created from CO oxidation above the curved surface at different surface temperatures and CO_2 partial pressure derived from integrated intensity of the PLIF signal versus surface temperature for both sides. c) Exemplary temperature dependence of O(1s) and C(1s) XP spectra measured at A- type, B-type, and apex. Figure reprinted with permission from reference[79].Copyright 2020, Wiley-VCH GmbH.

proximately 40 years. Two models in which steps play a crucial but different role had been suggested. One model was centered around the presence of an trapped molecular state for H_2 on (111) planes that would only lead to dissociation if the molecule would reach a step (defect) by ballistic diffusion. Only at the step would the molecule dissociate. The other model assumed two different (energy dependent) sticking probabilities for steps and terraces and did not invoke a long-lived molecular precursor and diffusion prior to dissociation. Measurement of the step density dependence of the dissociation probability at various incident energies for A- and B-type steps on *c*-Pt(111)[1$\bar{1}$0]-31° resolved that the latter model captures the dissociation characteristics. A linear dependence on step density over a very large step density range was found for the dissociation probability at low incident energy, being inconsistent with the former model. Also, the (mostly) surface temperature independence of the sticking probability and a step-type dependence (the B-type showing a higher reaction cross section than the A-type) for the dissociation probability disagreed with the first model.

CO OXIDATION

In recent years, the group of Ortega in collaboration with the Lundgren group (Lund, Sweden), has also undertaken research on chemical reactions on curved surfaces. Techniques such as near-ambient pressure XPS (NAP-XPS) and planar laser-induced fluorescence (PLIF) are there employed to study the effects of surface structure on surface chemistry away from UHV conditions. In this context, the correlation between surface changes on vicinal surfaces was explored in a series of publications on

CO chemisorption[65, 67] and oxidation[66, 79, 80] on curved crystals of transition metals.

The applicability of curved crystals at near-ambient pressure conditions was initially demonstrated for CO oxidation on a curved Pd sample (*c*-Pd(111)[1$\bar{1}$0]-30°) PLIF and XPS revealed step-type dependent differences in CO oxidation on Pd vicinals.[66, 80] The onset temperature for the transition from a low activity phase where CO poisons the surface to a high activity phase was found to be lower for B- than for A-type steps, and highest for (111) terraces. In contrast, the catalytic oxidation of CO at near ambient pressure on the curved Pt sample (*c*-Pt(111)[1$\bar{1}$0]-30°) showed no dependence on surface structure (or even reaction conditions).[79] There, NAP-XPS revealed that the uniform build-up of subsurface oxygen causes the simultaneous initiation of the reaction at all vicinal surfaces contained on the crystal. Figure 2.13, reprinted with permission from the original publication, shows the CO_2 PLIF signal before and after the onset of reaction, as well as XPS spectra of adsorbed species and reaction products.

CHIRAL REACTIONS

The potential of the naturally chiral surfaces on the dome shaped crystals as a purely structural form of enantioselectivity was further explored in a series of studies on the adsorption of chiral organic molecules. Using the dome as a high-throughput library of surface structures, the activity of decomposition of aspartic acid (Asp) was probed with spatially resolved XPS and adsorbate structures imaged by STM.[70] Surfaces with *(S)* chirality were found to be the least active towards decomposition of L-Asp, whereas in the case of D-Asp *(R)*-chiral surfaces were the least active, indicating that the adsorbed molecules were stabilised on these surfaces. By STM the adsorbed L-Asp was found to to adsorbed in rows rotated 20° from the close-packed directions on Cu(111). The adsorbate induced the facetting of steps into $\{320\}^S$ and $\{310\}^R$ microfacets, and the formation of Cu adatom islands with edges along the same directions. Surfaces on the dome that naturally exposed steps pre-aligned with the Asp rows were found to remain relatively straight while all other steps showed significant facetting. Both the reduced decomposition of adsorbed L-Asp and the facetting of steps on vicinal Cu into $\{320\}^S$ and $\{310\}^R$ microfacets thus indicated the energetic stabilisation of adsorbed L-Asp at these step facets. On the *d*-Cu(100)-10° crystal, the decomposition of both aspartic acid and tartaric acid (TA) in a surface explosion reaction was found to have highly enantiospecific kinetics.[71] A 2D map of the reaction rate of TA decomposition on a *d*-Cu(110)-11° dome was subsequently used to determine the maximum in enatioselectivity, Cu(14 17 2)$^{R\&S}$.[81]

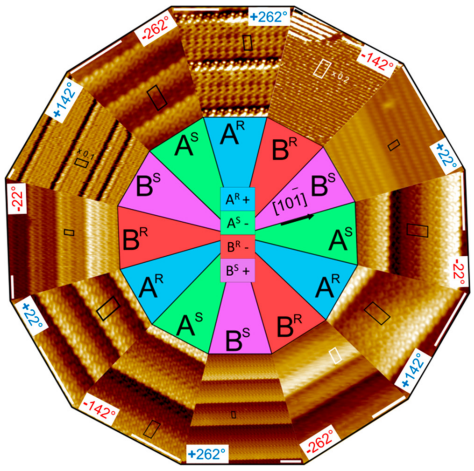

Figure 2.14: STM images of oxide formation on a dome-shaped *d*-Cu(111)-11° crystal. Angles indicate the rotational orientation of the oxide compared to (111), which corresponds to ± 22° with 120° increments. The predominant underlying Cu step type (A vs B) is indicated and the local chirality of kinks. Clearly, local orientation and surface chirality influence the chirality of the surface oxide. Figure reprinted with permission from reference [73]. Copyright 2020 American Chemical Society.

2.7.4. MAGNETIC, ELECTRONIC, AND CHEMICAL PROPERTIES OF FILMS GROWN ON CURVED CRYSTALS

In the late 1990's, the groups of Qiu and Bader (Berkeley, USA, and Argonne, USA) used crystals curved around the (001) plane of W, Ag, Cu, and Pd, as templates to grow stepped magnetic films (Fe or Co). As the steps on those films cause tuneable electron confinement on the nanometer scale, they were suited to systematically explore the quantum nature of short-range magnetic interactions, and the resulting magnetic properties, e.g. the magnetocrystalline anisotropy.

Initially, Kawakami *et al.* used two types of Ag crystalline samples to grow templated Fe films.[82] A 'fixed angle' (bifacial) crystal exposed the (001) surface on one half of a disk-shaped sample, the other half was polished to expose a stepped surface with a constant 6° vicinal angle. The second sample was a 'curved' crystal, where again half of a disk-shaped sample exposed (001), while the other half-disk was polished to smoothly curve to a 10° vicinal angle. Figure 2.15 shows the schematics of the bifacial curved crystals typically used by Qiu *et al.* The structure of Fe films grown on the Ag substrate were verified with LEED and RHEED. The surface magneto-optic Kerr effect (SMOKE) was used to examine the magnetic propertied. As SMOKE measurements were carried out using polarized light from a He-Ne laser, the beam spot size was inherently narrow (0.2 mm) enough to achieve sufficient spatial resolution on the 10 mm samples.

Measurements on 25 ML thick Fe films showed split loop hystereses on stepped surfaces when a magnetic field was applied perpendicular to the steps. These results

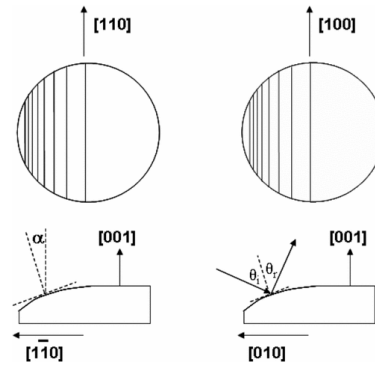

Figure 2.15: Schematic drawing of bifacial curved crystals, typically used in the work of Qiu *et al.*. Only part of the crystal's polished surfac is curved. Figure reprinted with permission from reference [83]. Copyright 2007 by the American Physical Society.

revealed, in addition to the Fe bulk anisotropy, the presence of a uniaxial in-plane magnetic anisotropy, caused by lattice symmetry breaking at the step edges. The easy axis was found to be parallel to the steps. The shift field H_s of the split loops was then used to determine the strength of the step-induced anisotropy at different points across the curvature of the sample. The anisotropy strength was found to depend quadratically on step density. This relation was explained by the Néel pair-bonding mechanism. In Néel's model, spin-orbit interactions influence the magnetic anisotropy through nearest neighbor electronic hybridization. Missing bonds at the step edges could thus locally change the hybridization and cause the anisotropy.

Additionally, a wedge of thinner Fe films was grown on the bifacial substrate. The critical thickness of the spin-reorientation transition from perpendicular magnetization to the in-plane magnetization found at thicker films was then determine for the two sides of the crystal. There, Fe on the 6° vicinal surface showed a higher critical thicknesses than on the (001) surface, indicating that steps stabilized perpendicular magnetization.

The sensitivity of the magnetocrystalline anisotropy on lattice symmetry was explored in a subsequent study by Choi et al.[84] Ultra-thin films (2 ML) of Fe were grown on a W(001) crystal, which similar to the previously described Ag sample, exposed (001) on half of the disk's surface, and on the other half curved around the [100] axis, from 0-9° vicinal angle. The spatial resolution of SMOKE experiments on the curved crystal was improved to 0.2° by placing a narrow slit in the beam path.

Both Fe and W crystallize in the *bcc* lattice, whereas Ag is a *fcc* metal, which has implications on the uniformity of the lattice mismatch between Fe films and the underlying substrate. Once again, the appearance of an in-plane uniaxial anisotropy was observed on stepped surfaces by SMOKE measurements, and increased quadratically with step density. In contrast to the first study on Ag, the easy-axis of the Fe

films on stepped W(001) was found perpendicular to the steps rather than parallel. The quadratic dependence on step density, while in line with the missing bond model (for bcc materials), could also be explained by biaxial strain of the *bcc* layer on the *fcc* substrate.

To further study the magnetic behavior, the effect of the anisotropy strength on film thickness was explored. Growing Fe wedges on the curved crystal made it possible to tune both vicinal angle and Fe layer thickness. However, the anisotropy strength was found to only depend weakly on the film thickness. A $1/d$ dependence, as expected for a surface-type anisotropy, could not be confirmed. While the authors discussed that a lattice mismatch may introduce a volume-type anisotropy an thus contribute to the anisotropy strength, no definite conclusions regarding the origin of the anisotropy could be made. In the Néel model, both biaxial strain, as well as the missing bonds could explain the quadratic dependence.

The role of biaxial strain could conclusively be dismissed in a study of magnetic Co layers on a curved Cu(001) crystal.[85] A Co layer (8 ML thickness) was dosed on a Cu(001) crystal, with half its surface curved up to 6° around the $[1\bar{1}0]$ axis. The step-induced magnetic anisotropy in the Co films was found to depend linearly on step density, as predicted for the effect of missing bonds in stepped *fcc* films by the Néel model. This linear dependence could not originate from biaxial strain. Furthermore, dosing partial coverages of Cu on the Co films caused suppression of the step-induced anisotropy, if the dosed Cu was able to diffuse to the Co step edges. Magnetic switching varied linearly with step density and occurred at doses where complete Cu rows could be formed at the step edges. The formation of horizontal Co-Cu bonds at the steps suppressing the step-induced anisotropy further confirmed the role of missing bonds as the origin of this anisotropy.

Remarkably, Fe films on a curved *fcc* Pd(001) template showed a linear dependence of the step-induced, in-plane anisotropy,[86] rather than the quadratic dependence that was observed for the Fe/Ag(001) and Fe/W(001) systems and predicted for *bcc* lattices. The additional effect for the Fe/Pd system is the strong spin-orbit interaction in Pd, which causes polarization at the interface and an induced magnetic moment in the topmost Pd layers. As a result, the observed step-induced anisotropy was 3 times larger than in the previously described systems. The anisotropy was thus dominated by the effect of the induced magnetic moment at the Pd step edges, rather than the magnetization of the Fe film, causing the *fcc*-like linear dependence of anisotropy strength on step density. Additionally, the induced magnetic moment caused an increase in the Curie temperature (T_C) of stepped Fe layers < 2 ML.

In a follow-up study in 2008, studying Fe films grown on a curved Pt(111) sample, a similar effect was observed.[87, 88] The strong induced ferromagnetic moment at the Fe/Pt interface resulted in a step-induced anisotropy that scaled with a power of 4

with step density. This strong anisotropy also enhanced the T_C of stepped Fe layers. While LEED had been applied to confirm the surface structure of the previously employed curved substrate crystals, this study provided a first STM image of the curved Pt crystal.

A large number of other systems were studied with an identical approach, e.g. Fe on curved Cr(001) [89–92], curved Ag(001) [93], and Pd(001) [94], Co on curved Cu(001) [95, 96], Ni on Cu(001) [97–99], NiO films on curved Ag(001) [100], and mixed FeMn/Co films on two types of curved Cu(001) [83].

In their first paper applying thin film growth on curved crystals, Ortega and coworkers recently exploited an additional benefit of these types of samples. Growing a wedge of Ag on a curved Au sample allowed variation of step density and film thickness on the same substrate.[101] The quantum-well states that are caused by confinement within the thin film of Ag were shown to scatter off steps at the Au/Ag interface. The Ag surface states on Au showed a more significant terrace-size confinement effect than in bulk Ag.

More recently, the San Sebastian group also started exploring other types of overlayers. Large-scale faceting occurred on a Ni crystal (*c*-Ni(111)[1$\bar{1}$0]-30°) when instead of terminating to vacuum, a hexagonal boronitride (hBN) layer was grown on the Ni surface.[102] However, step doubling, which occured on the bare Ni surface,[64] was not observed on the hBN-covered crystal. Growing variable sizes of semiconducting hBN films is particularly interesting in regards to applications in microelectronic applications and fuel cells. The growth of templated hBN films was shown to induce structural changes in the underlying substrate. Structural changes on the A-type step side were observed by STM. Two phases forming a hill-and-valley structure were found: (111) terraces and (115) facets of a few nm in size. On the B-type step side of the apex, (111) terraces and (110) facets with an incommensurate overlayer of hBN are found. Both forms of facetting were explained as face segregations minimizing the elastic free energy. The differences in facetting across the curved crystal would then be determined by the interface energy between hBN and different vicinal Ni surfaces.

The electronic structure and chemical environment of the hBN layer was further determined using near edge x-ray absorption spectroscopy (NEXAFS), x-ray photoelectron spectroscopy (XPS), and ARPES, all using synchrotron radiation. For both sides of the apex, the hBN layer was found to be less strongly bound and, thus, further away from the Ni surface than on the (111) terraces. This appeared of significance during subsequent molecular oxygen (O_2) treatment.[103] After dissociation on the metal-like surface of hBN overlayer on Ni, two possible outcomes for creation of atomic oxygen appeared possible: oxygen intercalation and hBN oxidation. While the lat-

ter was found to be uniformly distributed along the crystal's curvature, intercalation increased with miscut angle, resulting in even weaker hBN-Ni binding.

The potential of employing curved crystal substrates to gain unprecedented structural control in surface spintronics was demonstrated in a recent study.[52] On two curved Ag surfaces featuring either close-packed or fully-kinked steps, Bi was deposited to form a $BiAg_2$ alloy film, which replicated the superlattice of the Ag substrate. Step edges of the alloys formed zig-zag step edges on the Ag sample with A- or B-type steps, and atomically straight step edges of the alloy on the Ag substrate with fully-kinked steps. This behavior indicates Bi-termination of the alloy at edges. The latter alloy showed quatization of the terrace widths at vicinal surfaces. Subsequently only the $BiAg_2$ film forming straight step edges was used to investigate helical Rashba states, which were exhibited energy shifts and changes in the spin-orbit coupling with step density. The authors attributed this behavior to coherent scattering in spin-textured helical Rashba states.

2.8. CONCLUSION

We believe that the previous discussion of the recent advances illustrates that curved single crystal surfaces can be very useful to both fundamental studies focusing on physical and chemical properties of surfaces and to more applied studies aiming to develop (thin layer) materials with particular properties. For such aims, they may be by far the easiest approach, e.g. when step density dependencies are at the focus of the study. For other aims, they may really be the only option, e.g. when subtle differences may be masked by quality or purity variations between multiple 'flat' single crystals.

Clearly, a thorough study of the exposed surface structures is in all cases crucial. LEED gives insight, but the combination with scanning probe techniques is preferred. As the latter are being applied commonly by now, the uncertainties regarding surface structure that still prevailed in the studies of the 20^{th} century, are not a major issue anymore. It may, however, require for each new surface to be studied at first a significant effort to find cleaning procedures that yield the desired (continuous) range of surface structures. This effort should not be underestimated.

While by now a significant number of metals have been used in curved single crystal shape, in comparison to the number of interesting pure metals and alloys, there is still much unexplored. Most studies so far used the coinage and Pt group metals. Also other materials, e.g. oxides may also be of interest to study with a crystal shape that exposes a curved surface. Studies on, e.g. TiO_2 and oxygen vacancies therein[104] and ZnO [105], are indeed now starting to appear. Hence, with fundamental aspects, e.g. the importance and quantification of diffusion of intermediates in chemical reactions and the use of chirality of surfaces to heterogeneous catalysis largely unex-

plored, curved crystals not yet finding their way into electrochemical studies, and their potential to aid in growth of particular 2D and thin layer materials barely having started, we expect that many studies employing curved samples are still to come.

REFERENCES

[1] C. R. Henry. Morphology of supported nanoparticles. *Progress in surface science*, 80(3-4):92–116, 2005.

[2] K. Besocke, B. Krahl-Urban, and H. Wagner. Dipole moments associated with edge atoms; A comparative study on stepped Pt, Au and W surfaces. *Surface Science*, 68:39–46, 1977.

[3] J. Moison and J. Domange. Substrate steps/adsorbed layer interaction; selective effect on the possible epitaxial relationships: Case of the S/Cu(111) system. *Surface Science*, 69(1):336–348, 1977.

[4] J. Moison and J. Domange. LEED study of all copper vicinal surfaces 4° off (100) and (111) planes under S, O and Pb adsorption. *Surface Science*, 97(1):1–15, 1980.

[5] M. Sander, R. Imbihl, and G. Ertl. Kinetic oscillations in catalytic CO oxidation on a cylindrical Pt single crystal surface. *The Journal of chemical physics*, 97(7):5193–5204, 1992.

[6] E. G. Linder. Photo-electric effect and surface structure in zinc single crystals. *Physical Review*, 30(5):649, 1927.

[7] K. Hausser and Scholz. Metall-Einkristalle. *Wiss. Veröff. a. d. SIEMENS-Konzern*, V(3):144, 1927.

[8] G. Tammann and F. Sartorius. Ätzerscheinungen am Kupfereinkristall. *Zeitschrift für anorganische und allgemeine Chemie*, 175(1):97–120, 1928.

[9] S. T. Martin. On the thermionic and adsorptive properties of the surfaces of a tungsten single crystal. *Physical Review*, 56(9):947, 1939.

[10] A. T. Gwathmey and A. F. Benton. The Growth, Orientation, and Preparation of the Surface of Single Crystals of Copper. *The Journal of Physical Chemistry*, 44(1):35–42, 1940.

[11] A. T. Gwathmey and A. F. Benton. The directional oxidation of a single crystal of copper by heating in air at reduced pressure. *The Journal of Chemical Physics*, 8(5):431–432, 1940.

[12] A. T. Gwathmey and A. F. Benton. The directional catalytic activity of a single crystal of copper. *The Journal of Chemical Physics*, 8(7):569–570, 1940.

[13] A. T. Gwathmey and A. F. Benton. The Reaction of Gases on the Surface of a Single Crystal of Copper. I. Oxygen. *The Journal of Physical Chemistry*, 46(8):969–980, 1942.

[14] H. Leidheiser Jr and A. T. Gwathmey. The Catalytic Reaction of Hydrogen and Oxygen on Plane Faces of a Single Crystal of Copper[1]. *Journal of the American Chemical Society*, 70(3):1200–1206, 1948.

[15] J. B. Wagner Jr and A. T. Gwathmey. The Formation of Powder and its Dependence on Crystal Face during the Catalytic Reaction of Hydrogen and Oxygen on a Single Crystal of Copper1. *Journal of the American Chemical Society*, 76(2):390–391, 1954.

[16] R. E. Cunningham and A. T. Gwathmey. The Influence of Foreign Atoms on the Surface Rearrangement Produced by the Catalytic Reaction of Hydrogen and Oxygen on a Single Crystal of Copper[1]. *Journal of the American Chemical Society*, 76(2):391–393, 1954.

[17] F. W. Young Jr, J. V. Cathcart, and A. T. Gwathmey. The rates of oxidation of several faces of a single crystal of copper as determined with elliptically polarized light. *Acta Metallurgica*, 4(2):145–152, 1956.

[18] K. R. Lawless and A. T. Gwathmey. The structure of oxide films on different faces of a single crystal of copper. *Acta metallurgica*, 4(2):153–163, 1956.

[19] H. Leidheiser Jr and A. T. Gwathmey. The Selective Deposition of Carbon on the (111) Face of a Nickel Crystal in the Catalytic Decomposition of Carbon Monoxide[1]. *Journal of the American Chemical Society*, 70(3):1206–1206, 1948.

[20] R. E. Cunningham and A. T. Gwathmey. 5 The Reaction of Hydrogen and Ethylene on Several Faces of a Single Crystal of Nickel. In *Advances in Catalysis*, volume 9, pages 25–36. Elsevier, 1957.

[21] A. T. Gwathmey, H. Leidheiser, and G. Smith. Friction and cohesion between single crystals of copper. *Proceedings of the Royal Society of London. Series A. Mathematical and Physical Sciences*, 212(1111):464–467, 1952.

[22] V. J. Kehrer and H. Leidheiser Jr. The Phase Transformation of Cobalt as Observed on Single Crystals. *The Journal of Chemical Physics*, 21(3):570–570, 1953.

[23] V. J. Kehrer Jr and H. Leidheiser Jr. The catalytic decomposition of carbon monoxide on large metallic single crystals. *The Journal of Physical Chemistry*, 58(7):550–555, 1954.

[24] H. Leidheiser Jr and F. H. Cook. The Anistropic Rate of Photographic Development of Single Crystals of Silver Chloride[1,2]. *Journal of the American Chemical Society*, 76(2):617–617, 1954.

[25] F. Hottier, J. Theeten, A. Masson, and J. Domange. Comparative LEED and RHEED examination of stepped surfaces; Application to Cu(111) and GaAs(100) vicinal surfaces. *Surface Science*, 65(2):563–577, 1977.

[26] W. Ranke, Y. Xing, and G. Shen. Orientation dependence of oxygen adsorption on a cylindrical GaAs sample: I. Auger measurements. *Surface Science*, 120(1):67–89, 1982.

[27] W. Ranke. Oxygen Adsorption on a Cylindrical GaAs Single Crystal Prepared by Molecular Beam Epitaxy. *Physica Scripta*, 1983(T4):100, 1983.

[28] W. Ranke and D. Schmeisser. Adsorption of water on a cylindrical silicon crystal. *Surface science*, 149(2-3):485–499, 1985.

[29] T. Gardiner, H. Kramer, and E. Bauer. The surface structure of the <110> zone of tungsten: A LEED and work function study. *Surface Science*, 112(1-2):181–196, 1981.

[30] W. Ellis and R. Schwoebel. LEED from surface steps on UO_2 single crystals. *Surface Science*, 11(1):82–98, 1968.

[31] S. Mróz and E. Bauer. The interaction of gold with the surface of a cylindrical tungsten single crystal. *Surface science*, 169(2-3):394–404, 1986.

[32] B. Pluis, A. D. Van der Gon, J. Frenken, and J. van der Veen. Crystal-face dependence of surface melting. *Physical review letters*, 59(23):2678, 1987.

[33] H. Hopster, H. Ibach, and G. Comsa. Catalytic oxidation of carbon monoxide on stepped platinum (111) surfaces. *Journal of Catalysis*, 46(1):37–48, 1977.

[34] J. Neugebohren, D. Borodin, H. W. Hahn, J. Altschäffel, A. Kandratsenka, D. J. Auerbach, C. T. Campbell, D. Schwarzer, D. J. Harding, A. M. Wodtke, et al. Velocity-resolved kinetics of site-specific carbon monoxide oxidation on platinum surfaces. *Nature*, 558(7709):280–283, 2018.

[35] A. Armitage, D. Woodruff, and P. Johnson. Crystallographic incident beam effects in quantitative Auger electron spectroscopy. *Surface Science*, 100(3):L483–L490, 1980.

[36] H.-T. Liu, A. Armitage, and D. Woodruff. Anisotropy of initial oxidation kinetics of nickel single crystal surfaces. *Surface science*, 114(2-3):431–444, 1982.

[37] A. Armitage and D. Woodruff. Initial adsorption kinetics of oxygen and sulphur on copper cylindrical crystal surfaces. *Surface Science*, 114(2-3):414–430, 1982.

[38] J. Arlow and D. Woodruff. Structural specificity of dissociative chemisorption of oxygen from molecular oxygen and from nitrous oxide on copper surfaces. *Surface Science*, 157(2-3):327–338, 1985.

[39] J. Arlow and D. Woodruff. Structural specificity in CO and H_2 oxidation over single crystal copper surfaces. *Surface science*, 180(1):89–109, 1987.

[40] M. Sander, M. Bassett, R. Imbihl, and G. Ertl. Spatial coupling between kinetic oscillations on different regions of a cylindrical Pt single crystal. *Vacuum*, 41(1-3):272–274, 1990.

[41] M. Sander, G. Veser, and R. Imbihl. Spirals and propagating reaction fronts during catalytic CO oxidation on a cylindrical Pt single crystal. *Journal of Vacuum Science & Technology A: Vacuum, Surfaces, and Films*, 10(4):2495–2500, 1992.

[42] G. Veser and R. Imbihl. Spatial pattern formation in the oscillatory NO + CO reaction on a Pt (100) surface and its vicinal orientations. *The Journal of chemical physics*, 96(9):7155–7163, 1992.

[43] G. Veser, P. A. Thiel, and R. Imbihl. Homogeneous and heterogeneous front nucleation in a bistable surface reaction: the NO + CO reaction on a cylindrical Pt crystal. *The Journal of Physical Chemistry*, 98(8):2148–2151, 1994.

[44] C. F. McFadden, P. S. Cremer, and A. J. Gellman. Adsorption of Chiral Alcohols on "Chiral" Metal Surfaces. *Langmuir*, 12(10):2483–2487, 1996.

[45] A. Ahmadi, G. Attard, J. Feliu, and A. Rodes. Surface reactivity at 'chiral' platinum surfaces. *Langmuir*, 15(7):2420–2424, 1999.

[46] S. J. Jenkins and S. J. Pratt. Beyond the surface atlas: A roadmap and gazetteer for surface symmetry and structure. *Surface Science Reports*, 62(10):373 – 429, 2007.

[47] A. J. Gellman. *Enantioselectivity on Naturally Chiral Metal Surfaces*, pages 75–95. Springer New York, New York, NY, 2010.

[48] G. A. Attard, A. Ahmadi, J. Feliu, A. Rodes, E. Herrero, S. Blais, and G. Jerkiewicz. Temperature effects in the enantiomeric electro-oxidation of D- and L-glucose on Pt$\{643\}^S$. *Journal of Physical Chemistry B*, 103(9):1381–1385, 1999.

[49] S. V. Auras, R. van Lent, D. Bashlakov, J. M. Piñeiros Bastidas, T. Roorda, R. Spierenburg, and L. B. F. Juurlink. Scaling Pt-catalyzed hydrogen dissociation on corrugated surfaces. *Angewandte Chemie International Edition*, 2020.

[50] S. V. Auras, R. A. B. van Bree, D. L. Bashlakov, R. van Lent, and L. B. F. Juurlink. It's not just the defects - a curved crystal study of H_2O desorption from Ag. *Physical Chemistry Chemical Physics*, 21(28):15422–15430, JUL 28 2019.

[51] A. De Alwis, B. Holsclaw, V. Pushkarev, A. Reinicker, T. Lawton, M. Blecher, E. Sykes, and A. Gellman. Surface structure spread single crystals (S^4C): preparation and characterization. *Surface science*, 608:80–87, 2013.

[52] J. E. Ortega, G. Vasseur, I. Piquero-Zulaica, J. Raoult, M. A. Valbuena, S. Schirone, S. Matencio, A. Mugarza, and J. Lobo-Checa. Atomically precise step grids for the engineering of helical states. *arXiv preprint arXiv:1902.05777*, 2019.

[53] T. Lawton, V. Pushkarev, E. Broitman, A. Reinicker, E. Sykes, and A. Gellman. Initial oxidation of Cu(hkl) surfaces vicinal to Cu(111): A high-throughput study of structure sensitivity. *The Journal of Physical Chemistry C*, 116(30):16054–16062, 2012.

[54] C. Hahn, J. Shan, Y. Liu, O. Berg, A. W. Kleijn, and L. B. Juurlink. Employing a cylindrical single crystal in gas-surface dynamics. *The Journal of Chemical Physics*, 136(11):114201, 2012.

[55] R. V. Mom, C. Hahn, L. Jacobse, and L. B. Juurlink. LEED analysis of a nickel cylindrical single crystal. *Surface Science*, 613:15–20, 2013.

[56] M. Henzler. LEED-investigation of step arrays on cleaved germanium (111) surfaces. *Surface Science*, 19(1):159–171, 1970.

[57] M. Van Hove and G. Somorjai. A new microfacet notation for high-Miller-index surfaces of cubic materials with terrace, step and kink structures. *Surface Science*, 92(2-3):489–518, 1980.

[58] F. Schiller, M. Corso, J. Cordón, F. G. de Abajo, and J. Ortega. Interplay between electronic states and structure during Au faceting. *New Journal of Physics*, 10(11):113017, 2008.

[59] M. Corso, F. Schiller, L. Fernández, J. Cordón, and J. Ortega. Electronic states in faceted Au(111) studied with curved crystal surfaces. *Journal of Physics: Condensed Matter*, 21(35):353001, 2009.

[60] J. E. Ortega, M. Corso, Z. Abd-el Fattah, E. Goiri, and F. Schiller. Interplay between structure and electronic states in step arrays explored with curved surfaces. *Physical Review B*, 83(8):085411, 2011.

[61] J. E. Ortega, J. Lobo-Checa, G. Peschel, S. Schirone, Z. A. El-Fattah, M. Matena, F. Schiller, P. Borghetti, P. Gambardella, and A. Mugarza. Scattering of surface electrons by isolated steps versus periodic step arrays. *Physical Review B*, 87(11):115425, 2013.

[62] J. E. Ortega, G. Vasseur, I. Piquero-Zulaica, S. Matencio, M. A. Valbuena, J. E. Rault, F. Schiller, M. Corso, A. Mugarza, and J. Lobo-Checa. Structure and electronic states of vicinal Ag(111) surfaces with densely kinked steps. *New Journal of Physics*, 20(7):073010, 2018.

[63] J. Janlamool, D. Bashlakov, O. Berg, P. Praserthdam, B. Jongsomjit, and L. B. Juurlink. Desorption of water from distinct step types on a curved silver crystal. *Molecules*, 19(8):10845–10862, 2014.

[64] M. Ilyn, A. Magaña, A. L. Walter, J. Lobo-Checa, D. G. de Oteyza, F. Schiller, and J. E. Ortega. Step-doubling at vicinal Ni(111) surfaces investigated with a curved crystal. *The Journal of Physical Chemistry C*, 121(7):3880–3886, 2017.

[65] A. L. Walter, F. Schiller, M. Corso, L. R. Merte, F. Bertram, J. Lobo-Checa, M. Shipilin, J. Gustafson, E. Lundgren, A. X. Bríon-Ríos, et al. X-ray photoemission analysis of clean and carbon monoxide-chemisorbed platinum (111) stepped surfaces using a curved crystal. *Nature communications*, 6(1):1–7, 2015.

[66] S. Blomberg, J. Zetterberg, J. Zhou, L. R. Merte, J. Gustafson, M. Shipilin, A. Trinchero, L. A. Miccio, A. Magaña, M. Ilyn, et al. Strain dependent light-off temperature in catalysis revealed by planar laser-induced fluorescence. *ACS Catalysis*, 7(1):110–114, 2017.

[67] F. Garcia-Martinez, F. Schiller, S. Blomberg, M. Shipilin, L. R. Merte, J. Gustafson, E. Lundgren, and J. E. Ortega. CO Chemisorption on Vicinal Rh(111) Surfaces Studied with a Curved Crystal. *The Journal of Physical Chemistry C*, 124(17):9305–9313, 2020.

[68] T. Nishizawa and K. Ishida. The Co (cobalt) system. *Bulletin of Alloy phase diagrams*, 4(4):387–390, 1983.

[69] A. J. Walsh, R. van Lent, S. V. Auras, M. A. Gleeson, O. T. Berg, and L. B. Juurlink. Step-type and step-density influences on CO adsorption probed by reflection absorption infrared spectroscopy using a curved Pt(111) surface. *Journal of Vacuum Science & Technology A: Vacuum, Surfaces, and Films*, 35(3):03E102, 2017.

[70] A. Reinicker, A. Therrien, T. Lawton, R. Ali, E. Sykes, and A. Gellman. Influence of step faceting on the enantiospecific decomposition of aspartic acid on chiral Cu surfaces vicinal to Cu {111}. *Chemical Communications*, 52(75):11263–11266, 2016.

[71] P. Kondratyuk, B. Karagoz, Y. Yun, and A. J. Gellman. Initiation of Vacancy-Mediated, Surface Explosion Reactions: Tartaric and Aspartic Acid on Cu Surfaces. *The Journal of Physical Chemistry C*, 123(31):18978–18985, 2019.

[72] J. R. Kitchin and A. J. Gellman. High-throughput methods using composition and structure spread libraries. *AIChE Journal*, 62(11):3826–3835, 2016.

[73] A. C. Schilling, A. J. Therrien, R. T. Hannagan, M. D. Marcinkowski, P. L. Kress, D. A. Patel, T. A. Balema, A. M. Larson, F. R. Lucci, B. P. Coughlin, R. Zhang, T. Thuening, V. Çınar, J.-S. McEwen, A. J. Gellman, and E. C. H. Sykes. Templated Growth of a Homochiral Thin Film Oxide. *ACS Nano*, 14(4):4682–4688, 2020.

[74] M. E. Turano, L. B. F. Juurlink, M. Gillum, E. Jamka, and D. R. Killelea. Oxygen Adsorption on Different Step Geometries of curved Ag(111). *submitted*.

[75] K. Cao, R. van Lent, A. W. Kleyn, M. Kurahashi, and L. B. Juurlink. Steps on Pt stereodynamically filter sticking of O_2. *Proceedings of the National Academy of Sciences*, 116(28):13862–13866, 2019.

[76] L. Jacobse, A. den Dunnen, and L. B. Juurlink. The molecular dynamics of adsorption and dissociation of O_2 on Pt (553). *The Journal of chemical physics*, 143(1):014703, 2015.

[77] C. Hahn. *Steps away from flat land*. PhD thesis, Leiden University, Leiden, the Netherlands, 2015.

[78] R. van Lent, S. V. Auras, K. Cao, A. J. Walsh, M. A. Gleeson, and L. B. Juurlink. Site-specific reactivity of molecules with surface defects—The case of H_2 dissociation on Pt. *Science*, 363(6423):155–157, 2019.

[79] F. Garcia-Martinez, C. García-Fernández, J. P. Simonovis, A. Hunt, A. Walter, I. Waluyo, F. Bertram, L. R. Merte, M. Shipilin, S. Pfaff, S. Blomberg, J. Zetterberg, J. Gustafson, E. Lundgren, D. Sánchez-Portal, F. Schiller, and J. E. Ortega. Catalytic Oxidation of CO on a Curved Pt(111) Surface: Simultaneous Ignition at All Facets through a Transient CO-O Complex**. *Angewandte Chemie International Edition*, 59(45):20037–20043, 2020.

[80] F. Schiller, M. Ilyn, V. Pérez-Dieste, C. Escudero, C. Huck-Iriart, N. Ruiz del Arbol, B. Hagman, L. R. Merte, F. Bertram, M. Shipilin, S. Blomberg, J. Gustafson, E. Lundgren, and J. E. Ortega. Catalytic Oxidation of Carbon Monoxide on a Curved Pd Crystal: Spatial Variation of Active and Poisoning Phases in Stationary Conditions. *Journal of the American Chemical Society*, 140(47):16245–16252, 2018.

[81] B. Karagoz, M. Payne, A. Reinicker, P. Kondratyuk, and A. J. Gellman. A Most Enantioselective Chiral Surface: Tartaric Acid on All Surfaces Vicinal to Cu(110). *Langmuir*, 35(50):16438–16443, 2019. PMID: 31729881.

[82] R. Kawakami, E. J. Escorcia-Aparicio, and Z. Qiu. Symmetry-induced magnetic anisotropy in Fe films grown on stepped Ag(001). *Physical review letters*, 77(12):2570, 1996.

[83] J. Choi, J. Wu, Y. Wu, C. Won, A. Scholl, A. Doran, T. Owens, and Z. Qiu. Effect of atomic steps on the interfacial interaction of Fe Mn/ Co films grown on vicinal Cu(001). *Physical Review B*, 76(5):054407, 2007.

[84] H. J. Choi, Z. Qiu, J. Pearson, J. Jiang, D. Li, and S. Bader. Magnetic anisotropy of epitaxial Fe films grown n on curved W(001) with a graded step density. *PHYSICAL REVIEW-SERIES B-*, 57:R12–713, 1998.

[85] R. Kawakami, M. Bowen, H. J. Choi, E. J. Escorcia-Aparicio, and Z. Qiu. Effect of atomic steps on the magnetic anisotropy in vicinal Co/Cu(001). *Physical Review B*, 58(10):R5924, 1998.

[86] H. J. Choi, R. Kawakami, E. J. Escorcia-Aparicio, Z. Qiu, J. Pearson, J. Jiang, D. Li, and S. Bader. Curie temperature enhancement and induced Pd magnetic moments for ultrathin Fe films grown on stepped Pd(001). *Physical review letters*, 82(9):1947, 1999.

[87] R. Cheng, S. Bader, and F. Fradin. Magnetic properties of Fe on vicinal Pt(111). *Journal of Applied Physics*, 103(7):07B729, 2008.

[88] R. Cheng, S. Bader, and F. Fradin. Strong magnetic surface anisotropy of ultrathin Fe on curved Pt(111). *Physical Review B*, 77(2):024404, 2008.

[89] E. J. Escorcia-Aparicio, H. J. Choi, W. Ling, R. Kawakami, and Z. Qiu. The effect of interfacial steps on the ferromagnetic/antiferromagnetic interface of thin Fe films on Cr[001]. *IEEE transactions on magnetics*, 34(4):1219–1221, 1998.

[90] E. J. Escorcia-Aparicio, H. J. Choi, W. Ling, R. Kawakami, and Z. Qiu. 90° Magnetization Switching in Thin Fe Films Grown on Stepped Cr(001). *Physical review letters*, 81(10):2144, 1998.

[91] E. J. Escorcia-Aparicio, H. J. Choi, J. Wolfe, W. Ling, R. Kawakami, and Z. Qiu. Modification of the magnetic properties of Fe/Cr(001) by controlling the compensation of a vicinal Cr(001) surface. *Journal of applied physics*, 85(8):4961–4963, 1999.

[92] E. J. Escorcia-Aparicio, J. Wolfe, H. J. Choi, W. Ling, R. Kawakami, and Z. Qiu. Magnetic phases of thin Fe films grown on stepped Cr(001). *Physical Review B*, 59(18):11892, 1999.

[93] Y. Wu, C. Won, and Z. Qiu. Magnetic uniaxial anisotropy of Fe films grown on vicinal Ag(001). *Physical Review B*, 65(18):184419, 2002.

[94] H. J. Choi, R. Kawakami, E. J. Escorcia-Aparicio, Z. Qiu, J. Pearson, J. Jiang, D. Li, R. Osgood III, and S. Bader. Magnetic properties of ultrathin Fe films grown on stepped W(001) and Pd(001) substrates. *Journal of applied physics*, 85(8):4958–4960, 1999.

[95] R. Kawakami, M. Bowen, H. J. Choi, E. J. Escorcia-Aparicio, and Z. Qiu. Step-induced magnetic anisotropy in Co/stepped Cu(001) as a function of step density and Cu step decoration. *Journal of applied physics*, 85(8):4955–4957, 1999.

[96] Y. Wu, C. Won, H. Zhao, and Z. Qiu. Surface magneto-optic Kerr effect study of Co thin films grown on double curved Cu(001). *Physical Review B*, 67(9):094409, 2003.

[97] U. Bovensiepen, H. J. Choi, and Z. Qiu. Step-induced magnetic anisotropy in vicinal Ni/Cu(001) and its effect on the spin-reorientation transition. *Physical Review B*, 61(5):3235, 2000.

[98] H. Zhao, Y. Wu, C. Won, F. Toyoma, and Z. Qiu. Effect of the Cu capping layer on the magnetic anisotropy of Ni/Cu(100). *Physical Review B*, 66(10):104402, 2002.

[99] U. Bauer, J. Choi, J. Wu, H. Chen, and Z. Qiu. Effect of step decoration on the spin reorientation of Ni films grown on vicinal Cu(001). *Physical Review B*, 76(18):184415, 2007.

[100] Y. Wu, Z. Qiu, Y. Zhao, A. Young, E. Arenholz, and B. Sinkovic. Tailoring the spin direction of antiferromagnetic NiO thin films grown on vicinal Ag(001). *Physical Review B*, 74(21):212402, 2006.

[101] F. Schiller, Z. A. El-Fattah, S. Schirone, J. Lobo-Checa, M. Urdanpilleta, M. Ruiz-Osés, J. Cordón, M. Corso, D. Sánchez-Portal, A. Mugarza, et al. Metallic thin films on stepped surfaces: lateral scattering of quantum well states. *New Journal of Physics*, 16(12):123025, 2014.

[102] L. Fernandez, A. A. Makarova, C. Laubschat, D. V. Vyalikh, D. Y. Usachov, J. E. Ortega, and F. Schiller. Boron nitride monolayer growth on vicinal Ni(111) surfaces systematically studied with a curved crystal. *2D MATERIALS*, 6(2), APR 2019.

[103] A. A. Makarova, L. Fernandez, D. Y. Usachov, A. Fedorov, K. A. Bokai, D. A. Smirnov, C. Laubschat, D. V. Vyalikh, F. Schiller, and J. E. Ortega. Oxygen Intercalation and Oxidation of Atomically Thin h-BN Grown on a Curved Ni Crystal. *The Journal of Physical Chemistry C*, 123(1):593–602, 2019.

[104] L. A. Miccio, M. Setvin, M. Müller, M. Abadía, I. Piquero, J. Lobo-Checa, F. Schiller, C. Rogero, M. Schmid, D. Sánchez-Portal, U. Diebold, and J. E. Ortega. Interplay between Steps and Oxygen Vacancies on Curved TiO_2(110). *Nano Letters*, 16(3):2017–2022, 2016.

[105] E. Grånäs, B. Arndt, C. Seitz, M. Wagstaffe, and A. Stierle. Atomic scale step structure and orientation of a curved surface ZnO single crystal. *The Journal of Chemical Physics*, 152(7):074705, 2020.